Mixed-mode oscillations and twin canard orbits in an autocatalytic chemical reaction

Cris R. Hasan [1], Bernd Krauskopf [1], Hinke M. Osinga [1]

Abstract

A mixed-mode oscillation (MMO) is a complex waveform with a pattern of alternating small-amplitude oscillations (SAOs) and large-amplitude oscillations (LAOs). MMOs have been observed experimentally in many physical and biological applications, but most notably in chemical reactions. We are interested in MMOs of an autocatalytic chemical reaction that can be modeled by a system of three ordinary differential equations with one fast and two slow variables. This difference in time scales provides a mechanism for generating small and large oscillations. Provided the time-scale ratio ε is sufficiently small, Geometric Singular Perturbation Theory predicts the existence of two-dimensional locally invariant manifolds called slow manifolds. Slow manifolds and their intersections, which occur along so-called canard orbits, give great insight into the mechanisms for generating SAOs. The mechanisms for LAOs are less well understood and involve analysis of the global dynamics. We study the autocatalytic reaction model in a parameter regime with ε relatively large and observe very complex behavior. We find that for larger values of ε, the structure of the slow manifolds is more intricate than what is predicted by the theory for sufficiently small ε. Canard orbits in this parameter regime are organized in pairs that have the same number of SAOs. Our results suggest a mechanism where SAOs transform into LAOs and change the geometry of global returns in MMOs.

Key words

Mixed-mode oscillations, slow manifolds, twin canard orbits, autocatalator, multiple time scales.

1 Introduction

A trajectory that exhibits a combination of small-amplitude oscillations (SAOs) and large-amplitude oscillations (LAOs) is called a mixed-mode oscillation (MMO) [9]. Such oscillations have been observed in many applications, including semiconductor lasers [2, 27], neuron models [14, 19, 28, 40] and chemical reactions [24, 35, 36]. Fig. 1 shows two examples of periodic MMOs that are generated by the model studied in this paper; see already system Eq. (1). Panel (a) shows an MMO with one LAO and four SAOs, and panel (b) shows an MMO with one LAO followed by one SAO, another LAO, and then two SAOs. One says that the *signature* of the MMO in panel (a) is 1^4, and that of the MMO in panel (b) is $1^1 1^2$. Generally, a periodic MMO with signature ${L_1}^{s_1} {L_2}^{s_2}\ldots$, consists of L_1 LAOs, s_1 SAOs, L_2 LAOs, s_2 SAOs and so on.

We are interested in MMOs that arise in systems with multiple time scales, more specifically, in systems with one fast and two slow variables. MMOs in such slow-fast systems have been widely investigated in recent years; see the recent survey [9]. Geometric Singular Perturbation Theory (GSPT) exploits the separation of different time scales in order to explain

[1]Department of Mathematics, The University of Auckland, New Zealand. corresponding author: cris.hasan@auckland.ac.nz

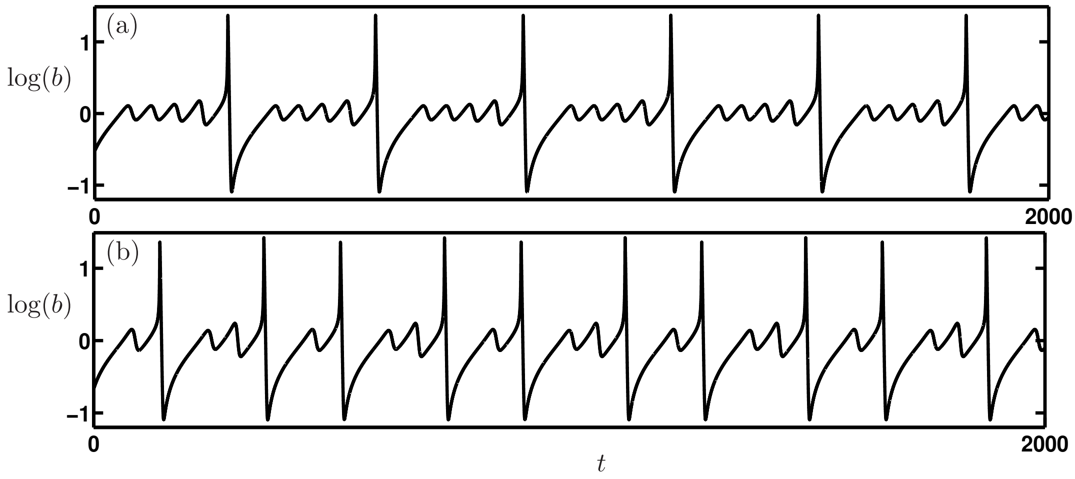

Figure 1: Two different periodic MMOs for system Eq. (1), with time series of signature 1^4 for $\mu = 0.295$ (a) and of signature $1^1 1^2$ for $\mu = 0.2975$ (b).

the complex dynamics of slow-fast systems [4, 5, 7, 15, 25, 42, 44]. The approach taken is geometric in nature and goes back to work by Fenichel [15] from 1979. Fenichel proved the existence of slow manifolds as perturbations of the so-called critical manifold, which exists in the singular limit as the time-scale ratio ε goes to 0; here it is assumed that ε is sufficiently small. In systems with one fast and two slow variables, slow manifolds are locally invariant two-dimensional manifolds that can be either attracting or repelling. Their intersections are called canard orbits. A considerable amount of analysis of canard orbits has been performed, e.g., in [7, 42, 44], and numerical methods to compute slow manifolds and their intersections have been developed in [10, 11, 12]. The upshot is that mechanisms for generating SAOs can be explained with methods from GSPT, but the mechanisms for LAOs need further analysis; see also [9] as an entry point to the literature.

The focus of this paper is a prototypical model of an autocatalytic chemical reaction that features one fast and two slow variables. This model was first introduced by Petrov, Scott, and Showalter [36] as an extension of the classical two-dimensional autocatalator [16, 32]. Initial studies reported on the existence of chaotic dynamics, but the oscillations in this system were later identified as MMOs [33, 34]. The underlying mechanisms for generating the SAOs in the autocatalator model and their parameter dependence have also been studied further in [22]. We are particularly interested in the autocatalator system because its critical manifold has an unusual shape that does not provide an obvious explanation of how LAOs are generated. Our goal is to study the transitions from SAOs to LAOs and explain in more detail the geometry underlying the dependence of the MMO signature on parameters. The autocatalator system is given by

$$\left\{\begin{array}{rcl} \dot{a} & = & \varepsilon\,(\mu\,(\kappa + c) - a\,b^2 - a), \\ \dot{b} & = & a\,b^2 + a - b, \\ \dot{c} & = & \varepsilon\,(b - c), \end{array}\right. \tag{1}$$

where we use the same notation as in [22]. The variables $a, b, c \in \mathbb{R}^+$ represent dimensionless concentrations of abstract chemical reactants. The model is called the autocatalator because the catalyst of the reaction, the substance b in Eq. (1), is also a product of the reaction;

a catalyst is a substance that increases the rate of the chemical reaction without undergoing any permanent chemical change. The main bifurcation parameter $\mu > 0$ represents the dimensionless constant concentration of the so-called pool chemical species [38] and κ represents the constant rate of the initiation reaction. The parameter ε is the time-scale ratio that is chosen to have small positive values ($0 < \varepsilon \ll 1$); this implies that b is a fast variable, and a and c are slow variables.

Milik and Szmolyan [33, 34] studied system Eq. (1) with $\kappa = 2.5$ and $\varepsilon = 0.01$, and we use the same parameter values, except in Section 4 where we vary ε. They used GSPT and blow-up techniques to prove the existence of canard orbits in Eq. (1) in the neighborhood of a so-called folded singularity located on the curve along which the repelling and attracting sheets of the critical manifold meet. Guckenheimer and Scheper [22] studied system Eq. (1) in the same parameter regime. They investigated the transitions between MMOs as μ is varied by constructing an induced return map defined on a one-dimensional domain near the folded singularity; they found that this map captures the dynamics of the system qualitatively as well as quantitatively.

We complement the previous studies by elucidating the local and global geometric mechanism for the observed MMOs in the three-dimensional phase space of system Eq. (1). The novelty of our research is that we study the geometry of the interaction of two-dimensional slow manifolds globally in phase space. Hence, we consider the canard orbits as part of trajectories that may involve both slow and fast epochs. As a consequence, we find that the time-scale ratio $\varepsilon = 0.01$ is too large for a straightforward application of known results from GSPT; in particular, we find many more canard orbits than predicted by GSPT for small ε. To understand the underlying geometric structure of the slow manifolds and canard orbits, we use advanced numerical methods that are based on a boundary value problem setup [10, 11, 12]. Our computations indicate that slow manifolds and canard orbits still generate a mechanism for SAOs, but we also observe complex behavior that does not appear for sufficiently small ε. In particular, we find that canard orbits are organized in pairs that exhibit the same number of SAOs. We call such paired canard orbits *twin canard orbits*. We also observe that twin canard orbits divide the attracting slow manifold into separate regions that we call ribbons. Their significance is that all orbits on a ribbon have the same number of SAOs; moreover, in between ribbons with successively larger numbers of SAOs, we find further ribbons with more complicated signatures.

We present a new computational setup that enables us to detect all possible canard orbits in a systematic way. In contrast to the standard approach of detecting intersections between the repelling and attracting slow manifolds in a section near the folded singularity, we compute orbit segments on the attracting slow manifold up to a section that lies far away from the singularity and is transverse to the critical manifold; far away from the folded singularity, the critical manifold is a good approximation of the repelling slow manifold, so that the canard orbits are easily identified as those orbit segments that end on the critical manifold. Far away from the folded singularity, it is also possible to choose the section such that it is transverse to the flow locally near the critical manifold. This means that each canard orbit is uniquely identified by its intersection point with the critical manifold.

It is straightforward to distinguish SAOs from LAOs in Fig. 1. However, there is no standard criterion for determining whether the amplitude of a given oscillation is small or large. Therefore, we introduce a practical heuristic criterion to distinguish between SAOs and LAOs. We continue the canard orbits in ε in order to understand the mechanism behind the termination of twin canard orbits and the transitions between different MMO signatures, that is, transitions from SAOs to LAOs. The continuation of canard orbits in ε has been demonstrated for two other models [12, 20]. In this paper, we show that the overall structure of the continuation of canard orbits of the autocatalator Eq. (1) is very complicated. Certain canard orbits can be continued towards the limit of $\varepsilon = 0$, and we find that these have the properties that are predicted by the known theory of folded singularities. When continuing canard orbits in the other direction, we encounter fold bifurcations that give rise to twin canard orbits; such fold bifurcations correspond to (generic) quadratic tangencies between the attracting and repelling slow manifolds. We illustrate this type of tangency in the combined phase and parameter space.

This paper is organized as follows. Section 2 briefly reviews earlier findings for system Eq. (1) and then presents further analysis of the system. We start with the bifurcation diagram, which shows the transitions between different signatures of MMOs as μ varies. This is followed by a short review of GSPT with regard to system Eq. (1). In Section 3, we present numerical results that reveal very complex objects which do not exist near the limit of $\varepsilon = 0$. We construct a flow map in order to detect all canard orbits and capture the global aspects of the dynamics. Section 4 gives details about the mechanism for termination/creation of twin canard orbits. We perform parameter continuation of the canard orbits and show how twin canard orbits terminate at fold bifurcations. The mechanism for this bifurcation is explained with a geometric illustration of how the attracting and repelling slow manifolds interact in parameter space. Section 5 summarizes the main findings of the paper and presents directions for future work.

2 Background on the autocatalator

We begin our analysis with exploring the bifurcation diagram of system Eq. (1) as μ is varied. Figure 2 shows the L_2-norm of equilibria (black curve) and periodic orbits (colored curves) versus μ; solid and dashed curves indicate stable and unstable branches, respectively. Note that there exists a single equilibrium for all values of μ. For $0 < \mu < 0.290510$, the equilibrium is stable. It undergoes a supercritical Hopf bifurcation (HB_1) at $\mu \approx 0.290510$ and becomes unstable before regaining stability at another supercritical Hopf bifurcation (HB_2) at $\mu \approx 0.796836$. In Fig. 2(a), a primary branch of stable periodic orbits (blue) emanates from HB_1 and terminates at HB_2. The primary branch increases rapidly in amplitude in the short interval $(0.2940, 0.3004)$. The sharp gain in amplitude is due to the phenomenon of canard explosion, which indicates that HB_1 is a so-called singular Hopf bifurcation [6, 17]. We are mainly interested in this parameter interval since it features mixed-mode oscillations (MMOs) and canard orbits. Figure 2(b) shows an enlargement for $\mu \in (0.2937, 0.3008)$ where periodic MMOs with different signatures coexist with the primary branch. The primary branch goes through period-doubling bifurcations at $\mu \approx 0.294449$ and $\mu \approx 0.300405$; hence, it appears dashed in the interval $\mu \in (0.294449, 0.300405)$. The first stable segment for $0.290510 < \mu < 0.294449$, is labeled 0^1 because the corresponding periodic orbit has oscillations of small amplitude only. The other stable segment, for $0.300405 < \mu < 0.3008$ is labeled 1^0 because the corresponding periodic orbit has oscillations of large amplitude only. The branch that emanates from the period-doubling bifurcations represents MMOs with signature 1^1 (cyan). There are twelve different types of MMOs that lie on isolated closed branches (isolas) of

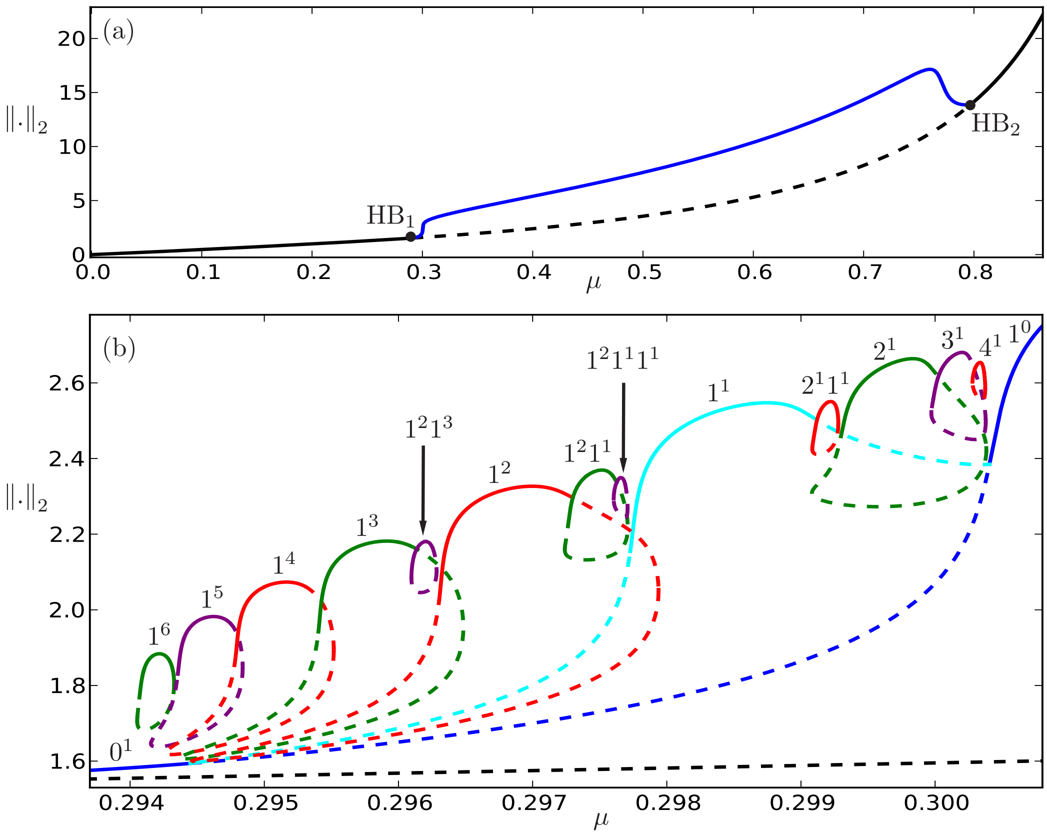

Figure 2: One-parameter bifurcation diagram of system Eq. (1) showing the L_2-norm versus μ. The black curve is the branch of equilibria and colored curves are branches of periodic orbits; the curves are solid when stable and dashed when unstable. Panel (b) is an enlargement near HB$_1$ that shows more branches which represent MMOs with different signatures.

periodic orbits. These isolas are alternately colored green, purple and red. Note that the top part of each branch is stable. Each isola goes through a number of saddle-node bifurcations of periodic orbits and period-doubling bifurcations. Therefore, different types of stabilities can be found along these isolas. Bistability can be found for some parameter values. For increasing values of μ, the number of large-amplitude oscillations (LAOs) increases and the number of small-amplitude (SAOs) decreases. Note that the signatures of the small branches labeled $1^2 1^1 1^1$, $2^1 1^1$ and $1^2 1^3$ are combinations of signatures of the neighboring branches [31, 43]. Stable branches of this bifurcation diagram were computed in [22] by continuing an approximated return map; we found two more branches, namely, $1^2 1^1 1^1$ and $1^2 1^3$. We also show the unstable branches that organize the different MMOs into overlapping isolas. Moreover, our calculations concern the actual periodic orbits of the full system Eq. (1).

The occurrence of SAOs in these periodic orbits can be explained by GSPT [15, 25, 42, 44]. We briefly review this theory here, where we use the stable MMO with signature 1^4 for $\mu = 0.295$ as a representative example; this MMO is denoted Γ.

First, the fast subsystem of system Eq. (1) is obtained by taking the limit as $\varepsilon \to 0$, which gives

$$\begin{cases} \dot{a} &= 0, \\ \dot{b} &= a\,b^2 + a - b, \\ \dot{c} &= 0. \end{cases} \tag{2}$$

Here, the slow variables a and c take the role of bifurcation parameters, and the dynamics is determined by the one-dimensional differential equation of the fast variable b. The equilibrium points of the fast subsystem define the critical manifold:

$$S := \left\{ (a, b, c) \in \mathbb{R}^3_+ \;\middle|\; a = \frac{b}{b^2 + 1} \right\},$$

which is a two-dimensional surface in $\mathbb{R}^3$. Note that S does not depend on c. The value of a is maximal when $b = 1$. Hence, S has two sheets, separated by the one-dimensional fold line

$$F := \left\{ (a, b, c) \in \mathbb{R}^3_+ \;\middle|\; b = 1, \text{ and } a = 0.5 \right\}.$$

The critical manifold, or a submanifold of S, is normally hyperbolic if each point on it corresponds to a hyperbolic equilibrium of the fast subsystem Eq. (2). We identify two such normally hyperbolic submanifolds; the attracting sheet

$$S^a := S \cap \{0 < b < 1\}, \tag{3}$$

and the repelling sheet

$$S^r := S \cap \{b > 1\}. \tag{4}$$

The dynamics of the slow variables is obtained by taking the limit as $\varepsilon \to 0$ after a time rescaling $t \mapsto \varepsilon\, t$, which gives

$$\begin{cases} \dot{a} &= \mu\,(\kappa + c) - a\,b^2 - a, \\ 0 &= a\,b^2 + a - b, \\ \dot{c} &= b - c, \end{cases}$$

where the differentiation is now with respect to the rescaled time. This is a system of differential algebraic equations that can be reduced to an explicit two-dimensional system on the critical manifold S in terms of the variables b and c. The equation for b is obtained via implicit differentiation of the algebraic equation, which is actually the equation for S. Hence, we have

$$\begin{cases} -(2\,a\,b - 1)\,\dot{b} &= (b^2 + 1)\,(\mu\,(\kappa + c) - a\,b^2 - a), \\ \dot{c} &= b - c, \end{cases} \tag{5}$$

where $a = b/(b^2 + 1)$. System Eq. (5) is called the reduced system. It is singular when $2\,a\,b - 1 = 0$, which is precisely when S has a fold with respect to the fast variable b. We desingularize system Eq. (5) via a non-constant time rescaling $t \mapsto -(2\,a\,b - 1)^{-1} t$ and obtain the desingularized reduced system

$$\begin{cases} \dot{b} &= (b^2 + 1)\,(\mu\,(\kappa + c) - a\,b^2 - a), \\ \dot{c} &= (-2\,a\,b + 1)\,(b - c), \end{cases} \tag{6}$$

with $a = b/(b^2 + 1)$, as before. The effect of the desingularization is that the direction of the flow is reversed on the repelling sheet S^r of S. Equilibria of system Eq. (6) that lie on the fold F of S are folded singularities; they are not equilibria of system Eq. (5). The (strong) stable manifold of such an equilibrium of system Eq. (6), if it exists, corresponds to a solution of system Eq. (5) that crosses from the attracting sheet S^a to the repelling sheet S^r; this solution is called the *(strong) singular canard*.

The term *singular canard* refers to a trajectory that crosses from S^a to S^r in the singular limit $\varepsilon = 0$. Singular canards give rise to a family of canard orbits for $\varepsilon > 0$ [4, 5], which are referred to as *maximal canards* in the literature and defined as the intersections between an attracting and a repelling slow manifold [42, 44]. We prefer the term *canard orbit*, because the term *canards* is generally reserved specifically for periodic orbits; see also [9].

For the remainder of the paper we consider Eq. (1) in the equivalent form

$$\begin{cases} \dot{a} &= \varepsilon\,(\mu\,(\kappa + c) - 10^{2B} a - a), \\ \dot{B} &= (10^B a + a\,10^{-B} - 1)/\ln(10), \\ \dot{c} &= \varepsilon\,(10^B - c). \end{cases} \tag{7}$$

where we use $B = \log(b)$ with base 10; this rescaling was also used in [22] to show the time series of the autocatalator. There are several advantages for using the rescaling $B = \log(b)$. First, it makes it more convenient to visualize the dynamics and allows for nicer presentations of manifolds. Moreover, this rescaling is very practical for computations because the variables a, B and c have about the same magnitude; this improves the stability of the computations. Note that the scaling does not have any influence on the qualitative nature of the phase portraits and, hence, on the location of bifurcations.

Figure 3 shows the critical manifold S (gray folded surface), which is divided by the fold line F into attracting and repelling sheets, S^a and S^r, respectively. Overlaid is the stable periodic orbit Γ (black) with its single LAO and four SAOs. The mechanism for SAOs of Γ is explained with GSPT by relating the dynamics of system Eq. (1) to the reduced system Eq. (5) and the corresponding desingularized system Eq. (6). For $\mu = 0.295$, the desingularized system Eq. (6) has an attracting equilibrium $p := \{(a, b, c) \mid a = 0.5,\ b = 1,\ c = 0.88983\}$, called a folded node, which lies on F. The strong stable manifold of p is the strong singular canard ξ_s, which is the green curve on S^a in Fig. 3. The folded node p (green dot) is located at the intersection of ξ_s and F. GSPT predicts that SAOs arise from the fact that the periodic orbit lands on S^a in the so-called funnel region, which is defined as the (smaller) wedge on S^a bounded by ξ_s and F. For sufficiently small ε, the distance from ξ_s at which the MMO lands on S^a in the funnel region determines the exact number of SAOs. However, Γ in Fig. 3 lands on S^a far to the right of the funnel region and does not appear to interact with p at all. We conclude that $\varepsilon = 0.01$ is too large for applying known results from GSPT to predict the number of SAOs of Γ. Hence, there must be another mechanism that organizes the SAOs of Γ.

To understand the mechanism for generating SAOs for (the larger value) $\varepsilon = 0.01$, we perform computations of slow manifolds. According to Fenichel's theorem [15, 25], a normally hyperbolic submanifold of S perturbs, under a sufficiently small perturbation $\varepsilon > 0$, to a slow manifold with the same smoothness and stability properties. Hence, there exist locally invariant perturbations of S^a and S^r, namely, attracting and repelling slow manifolds S^a_ε and S^r_ε, respectively. We use a boundary value problem setup, implemented in AUTO [13], to compute these slow manifolds; see [10, 11, 26] for more details. Each slow manifold is

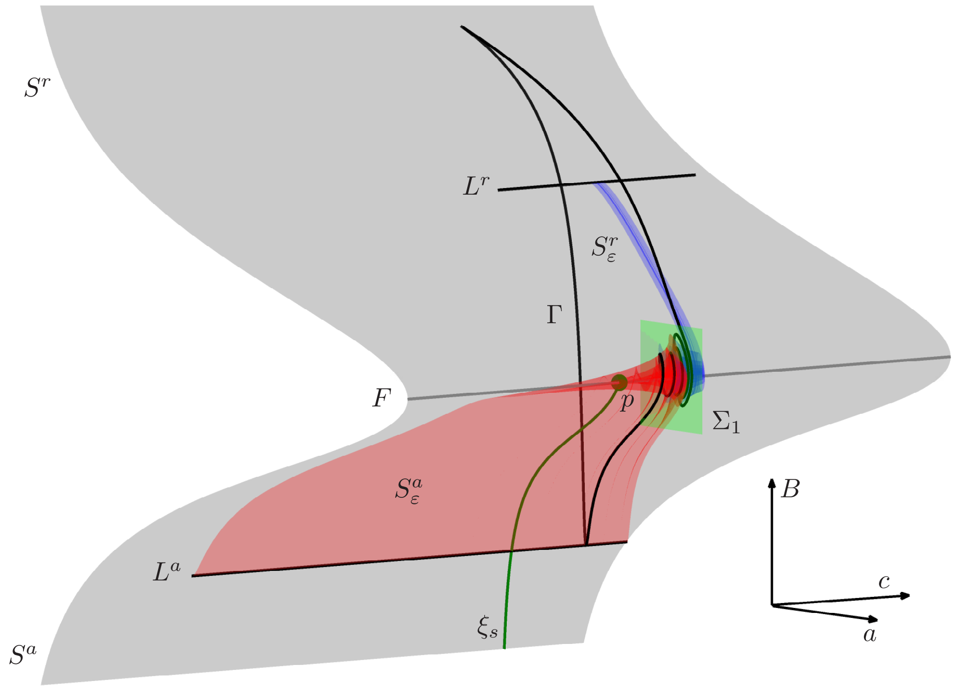

Figure 3: The periodic orbit Γ (black) with signature 1^4 plotted with the critical manifold (gray) and the slow manifolds for system Eq. (1) with $\mu = 0.295$. The attracting sheet S^a and the repelling sheet S^r of the critical manifold meet at the fold F (gray line). The attracting slow manifold S^a_ε (red) and repelling slow manifold S^r_ε (blue) are computed from L^a and L^r, respectively, up to the planar section Σ_1. The orbit ξ_s (green curve) is the strong singular canard and intersects F at the folded node p (green dot).

represented as a family of orbit segments that start on a line on S far away from F and end at a planar section transverse to F. Fenichel theory does not apply in the vicinity of $F \subseteq S$, but the slow manifolds extend under the flow as manifolds, and typically spiral around F (more specifically, around the weak eigendirection of p) [10, 42].

Figure 3 also illustrates the setup for computing the slow manifolds S^a_ε (red surface) and S^r_ε (blue surface). Both manifolds are computed as families of orbit segments that end in the planar section $\Sigma_1 := \{(a, B, c) \mid c = 1\}$ (green) transverse to F. The section Σ_1 is chosen further to the right of p so that we can detect as many canard orbits as possible. The attracting slow manifold S^a_ε starts on the line segment

$$L^a := \{(a, B, c) \mid a = 0.0799375,\ B = -1.094447\} \subseteq S^a,$$

which is chosen parallel to F such that $\Gamma \cap L^a \neq \emptyset$, that is, L^a contains the intersection point of Γ with S^a. The repelling slow manifold S^r_ε starts (in backward time) on the line segment

$$L^r := \{(a, B, c) \mid a = 0.191352,\ B = 0.705596\} \subseteq S^r,$$

which was chosen as follows. We tested different trajectories that start on S^r near F and end on S^r far away from F. We found that the trajectory that spends the longest time near S^r has a maximum with respect to B of $B \approx 0.705596$; we use this value to define L^r. These choices for L^a and L^r remain fixed when ε is varied in Section 4.

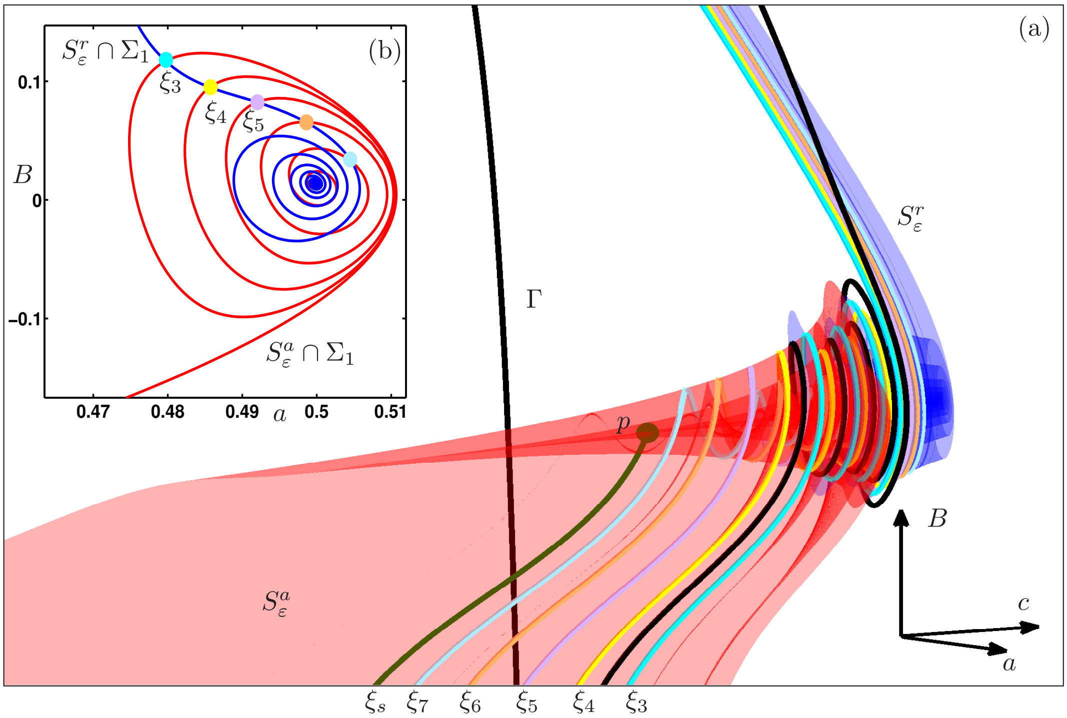

Figure 4: Panel (a) shows an enlargement of Fig. 3 with five canard orbits ξ_3–ξ_7 along with the strong singular canard ξ_s. Panel (b) shows the intersection curves of S^a_ε (red curve) and of S^r_ε (blue curve) with Σ_1. These two intersection curves intersect in a number of points, and the five intersection points ξ_3–ξ_7 are highlighted by five different colors. Each such intersection point in panel (b) corresponds to a canard orbit that is shown in panel (a) in the respective color.

Since L^a contains the intersection point of the periodic orbit Γ with S^a, we made sure that an entire segment of Γ lies on our approximation of S^a_ε as it begins its four SAOs before making a large excursion. The orbit Γ crosses the repelling sheet S^r of the critical manifold well above L^r and connects back to itself on S^a. In the limit as $B \to \infty$, the eigenvectors of the equilibria of the fast subsystem align with the tangent space of S^r. As a consequence, for any given fixed $\varepsilon > 0$ (e.g., $\varepsilon = 0.01$), the repelling slow manifold S^r_ε ceases to exist beyond sufficiently large finite values of B; see [23, 29, 33] for more details. This allows large oscillations to cross S^r eventually, leading to a global return to S^a_ε.

Figure 4 shows details of the interaction of S^a_ε and S^r_ε. Panel (a) is an enlargement of Fig. 3. The five colored curves labeled ξ_3–ξ_7 are intersections of S^a_ε and S^r_ε, that is, they are canard orbits. Figure 4(b) shows the intersection curves of S^a_ε and S^r_ε with the section Σ_1. Note that the curve $S^a_\varepsilon \cap \Sigma_1$ (red) intersects the curve $S^r_\varepsilon \cap \Sigma_1$ (blue) transversely in many points. Each point corresponds to a canard orbit lying on both S^a_ε and S^r_ε. Five of these intersection points are marked with differently colored dots. These points correspond to the canard orbits ξ_3–ξ_7 shown in Fig. 4(a). A given canard orbit is labeled ξ_i if it makes i SAOs in the vicinity of the fold F. Also, shown is the strong singular canard ξ_s (green) which does not lie on S^a_ε but rather on S^a. Note that canard orbits ξ_3–ξ_7 lie outside the funnel region; namely, they lie to the right of the strong singular canard. Nevertheless, Γ clearly lies on S^a_ε in between ξ_3 and ξ_4, which suggests that GSPT explains why Γ has four SAOs. Based on

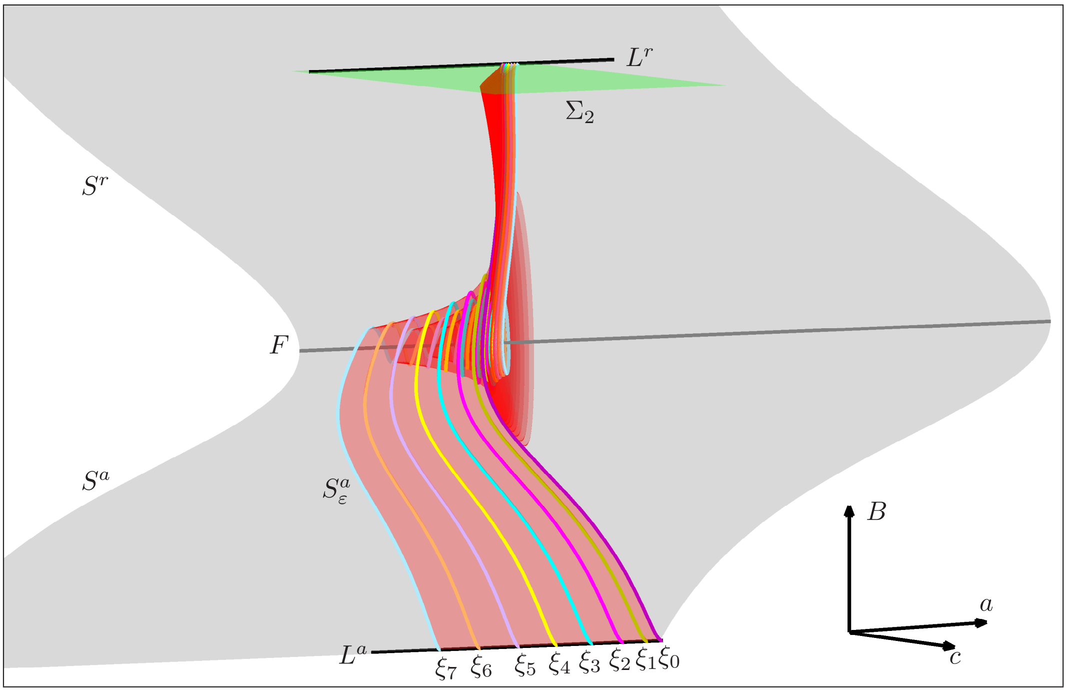

Figure 5: An extension of the attracting slow manifold S^a_ε (red) up to the section Σ_2 for the same parameter values as in Fig. 3. The eight canard orbits ξ_0–ξ_7 are shown in different colors.

the eigenvalues of the folded node p, the theory predicts that this folded singularity gives rise to two primary canard orbits and 29 secondary canard orbits near the singular limit [42, 44]. However, as we will discuss in Section 3, we find many more canard orbits for $\varepsilon = 0.01$; in fact, there are at least 68 canard orbits for this value of ε. Our findings suggest again that $\varepsilon = 0.01$ is too large for applying known results from GSPT to predict the total number of canard orbits.

3 Twin canard orbits and ribbons of the attracting slow manifold

We aim to explore the underlying complex behavior of system Eq. (7) and investigate how canard orbits are organized for relatively large values of ε. In order to detect all canard orbits in a systematic way, we extend the attracting slow manifold S^a_ε up to the section $\Sigma_2 := \left\{(a, B, c) \in \mathbb{R}^3_+ \mid B = 0.705596\right\}$, which is transverse to S^r and contains L^r far away from F. Figure 5 shows the extended manifold S^a_ε computed from L^a up to Σ_2. Here, canard orbits are detected as the trajectories on S^a_ε that terminate at L^r, which includes the canard orbits ξ_3–ξ_7 shown in Fig. 4. We show eight canard orbits in Fig. 5 that are labeled ξ_0–ξ_7, based on their number of SAOs. In particular, ξ_0 is the primary strong canard, which corresponds to the strong singular canard ξ_s in the limit as $\varepsilon \to 0$; namely, it separates trajectories on S^a_ε that make at least one rotation around F from those that escape the fold region without making any rotations. In other words, the canard orbit ξ_0 is the boundary between the region in which the attracting slow manifold S^a_ε has no rotations (jump region)

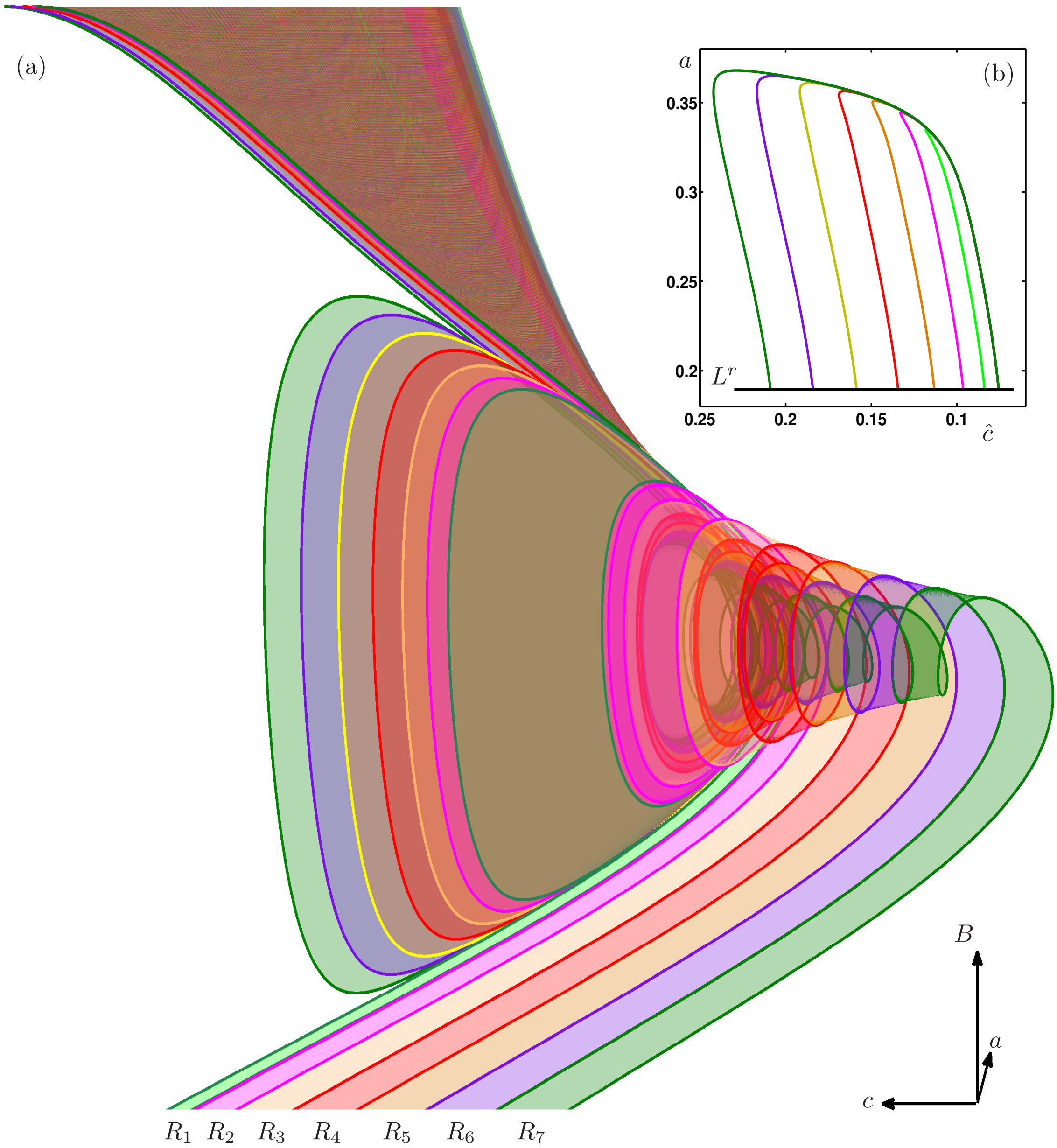

Figure 6: Ribbons of the extended attracting slow manifold S^a_ε of system Eq. (7) for the same parameter values as in Fig. 3. Panel (a) shows seven ribbons R_1–R_7 in different colors. Panel (b) shows the intersection curves of these ribbons with Σ_2 in their respective colors.

and the region with at least one rotation (no-jump region). Note that the primary strong canard ξ_0 as well as the secondary canard orbits ξ_1 and ξ_2 were not be detected with the standard computational approach presented in Fig. 4. On the other hand, all canard orbits ξ_0–ξ_2 are easily detected as trajectories that connect $L^a \subseteq S^a$ to $L^r \subseteq S^r$.

The extended slow manifold S^a_ε shown in Fig. 5 is not a single surface, but rather consists of separate surface segments that we call ribbons. Each ribbon is computed individually by starting from a canard orbit and sweeping along L^a until another canard orbit is detected. Figure 6 shows seven separate ribbons, denoted R_1 to R_7, of the extended attracting slow manifold S^a_ε in different shades of colors; the ribbons R_1–R_7 are shown individually in Fig. 7.

Each ribbon R_i is a family of trajectories that lie on S^a_ε and make i SAOs in the vicinity of the fold F. Figure 6(a) illustrates the global geometry of these ribbons. The ribbons are plotted up to Σ_2; however, note that the lower boundary of the figure is well above L^a. As the ribbons complete their respective number of SAOs they move away from F and fold over, reaching Σ_2 as doubled strips that are extremely close together. Figure 6(b) shows the intersection curves of the ribbons R_1–R_7 with Σ_2 in their respective colors. Here, we use the rescaled variable

$$\hat{c} = 10(c - (-0.97(a - 0.26) + 1.2)) \tag{8}$$

to make the intersection curves distinguishable. Note also that the horizontal axis increases to the left, which is consistent with the view in panel (a). The intersection curves shown in panel (b) are folded and nested, so that the folded curve that corresponds to R_i lies inside the folded curve corresponding to R_{i+1}. The end points of the folded intersection curves lie on L^r and have very close values of c. The end points of each curve $R_i \cap \Sigma_2$ correspond to a pair of canard orbits ξ_i and ξ'_i that exhibit the same number of SAOs and bound the ribbon R_i; see Fig. 7. We use the term *twin canard orbits* to describe such pairs ξ_i and ξ'_i. Figure 7 shows the geometry of the individual ribbons R_1–R_7. Note that each pair of twin canard orbits ξ_i and ξ'_i come very close together after making i SAOs. Each ribbon R_i rotates as a surface around F and makes i SAOs before reaching Σ_2.

The ribbons are more precise representatives for $\varepsilon = 0.01$ of the so-called *rotational sectors* defined in the GSPT literature for the singular limit as $\varepsilon \to 0$. A rotational sector I_i lies on the attracting sheet of the critical manifold and indicates the regime where orbit segments make i SAOs near F. For example, rotational sectors are used in [9, Section 3.1.1] to guarantee the existence of periodic MMOs with a particular signature 1^{s_1} that consist of one LAO and s_1 SAOs. To date, any rotational sector I_i has been thought of as being bounded by canard orbits ξ_i and ξ_{i-1} [9, 11, 40]. However, the boundary between two rotational sectors is more intricate and involves canard orbits with more complicated signatures; for example, see [9, Section 3.1.1]. As will be discussed next, in the present context, this translates to intermediate ribbons in between the ribbons of Figs. 6 and 7.

3.1 Global properties of ribbons

Now we consider the behavior of ribbons of the attracting slow manifold after crossing Σ_2. Figure 8 shows the global return of ribbon R_4; here R_4 was computed by extending the orbit segments in the family so that all have the same large arclength. Panel (a) shows the interaction between R_4 (red surface) with Σ_2 (green section) and how R_4 returns, as a surface, back to the vicinity of the attracting slow manifold near L^a. The red curve on Σ_2 is the closed intersection curve $R_4 \cap \Sigma_2$ and it lies almost on a straight line. Note that the extended ribbon R_4 forms a cap above Σ_2. After intersecting Σ_2 twice, R_4 make a global return to the vicinity of itself. The twin canard orbits ξ_4 and ξ'_4 (red orbits) bound the ribbon R_4. The periodic orbit Γ (black) lies on R_4 and intersects Σ_2 in two points. Figure 8(b) shows the intersection $R_4 \cap \Sigma_2$ (red curve) with the rescaled variable $\hat{c}$ on the horizontal axis so that the nature of the intersection curve becomes clear. It is important to realize that, for our choice of Σ_2, the line segment $L^r \subseteq \Sigma_2$ is the tangency locus that separates the two regions of Σ_2 where the flow is pointing transversally up ($\odot$) and down ($\otimes$) [30]. The red segment above L^r in Fig. 8(b) consists of the first returns of R_4 to Σ_2; the red segment below L^r consists of the second returns of R_4 to Σ_2, and it is the image of the upper red segment under the

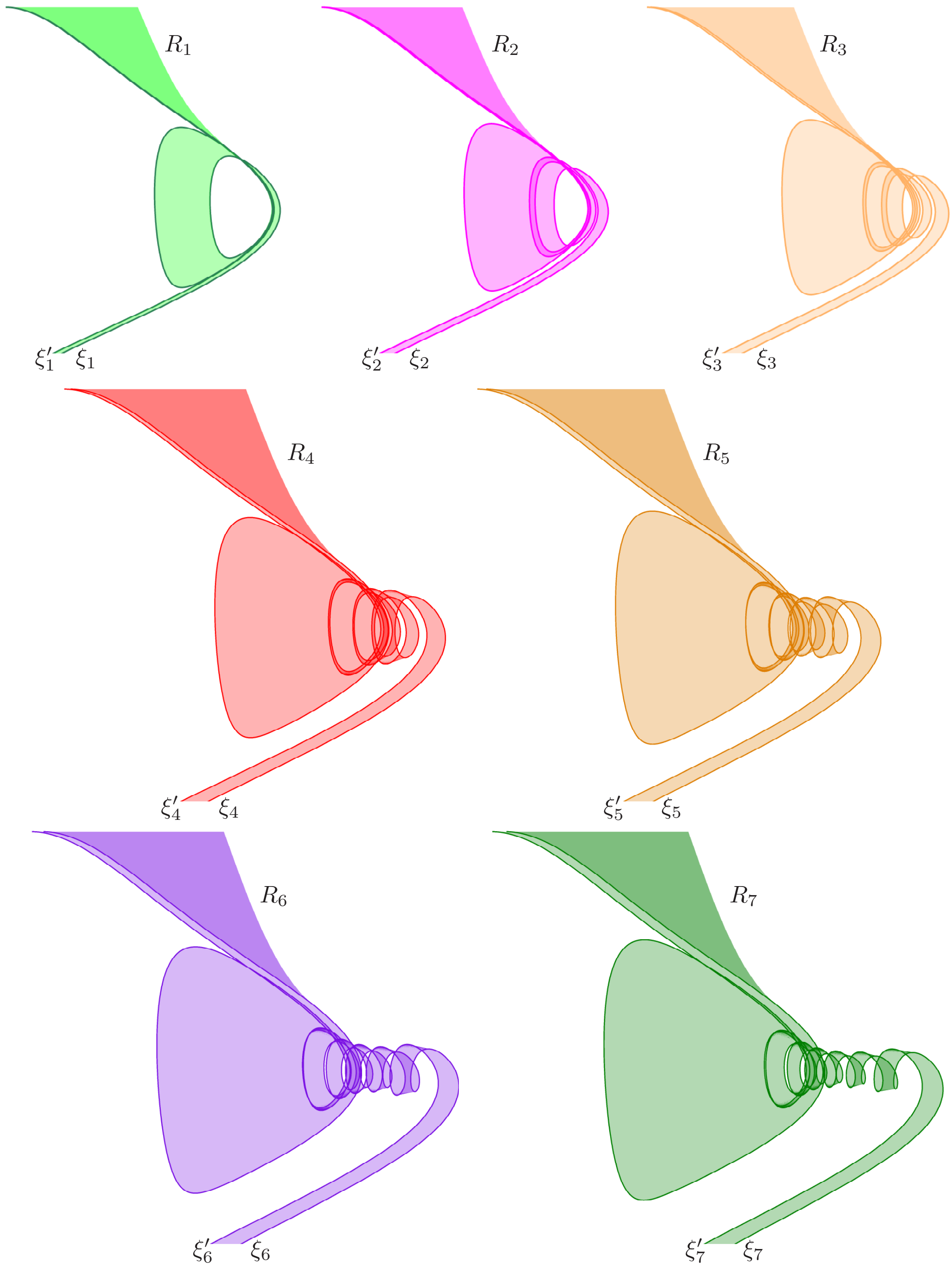

Figure 7: Individual ribbons R_1–R_7 of Fig. 6. Each ribbon R_i is bounded by twin canard orbits ξ_i and ξ_i' (thick curves).

flow. The intersection points of $R_4 \cap \Sigma_2$ with L^r correspond to the twin canard orbits ξ_4 and ξ_4'. The two black dots mark the intersection points of the periodic orbit Γ with Σ_2, which lie very close to the two local maxima of $\hat{c}$; it is not clear whether this is a coincidence or not. The behavior shown in Fig. 8 is representative of the other ribbons: ribbons R_1–R_7 also intersect Σ_2 in closed curves after their second returns (not shown). These closed curves are

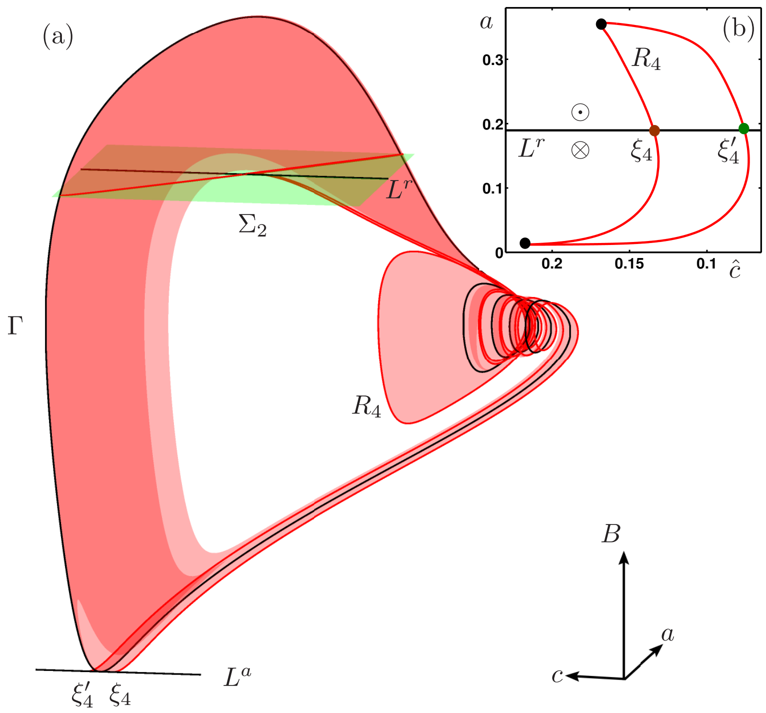

Figure 8: Global return of ribbon R_4 from Fig. 6. Panel (a) shows the extended ribbon R_4 (red). The two highlighted red orbits are the twin canards ξ_4 and ξ_4', and the black orbit is the periodic orbit Γ. The red curve in the green section Σ_2 is the closed intersection curve of R_4 with Σ_2. Panel (b) shows this curve using the rescaled variable $\hat{c}$. The line segment L^r is the tangency locus that separates the regions in which the flow is pointing up ($\odot$) and down ($\otimes$). The brown and green dots on L^r correspond to ξ_4 and ξ_4', respectively, and the two black dots correspond to Γ.

nested such that any closed curve that corresponds to R_i lies inside the curve corresponding to R_{i+1}; compare with Fig. 6(b), which shows only the curves of the first intersections.

In order to understand the global features of ribbons, Fig. 9 shows R_4 (red surface) extended up to its second intersection with Σ_2, as well as ribbon R_7 (green surface) extended up to its fourth intersection with Σ_2. Panel (a) shows how the extended ribbon R_7 makes a global return to the vicinity of R_4. The green curve on R_7 is a closed curve that is almost a straight line in Σ_2, and it corresponds to the third and fourth returns of R_7 to Σ_2. As before, twin canard orbits ξ_4 and ξ_4' (red orbits) bound the ribbon R_4, and the periodic orbit Γ (black) lies on R_4. Note that R_7 crosses Σ_2 twice before making a global return to the vicinity of R_4 and then intersects Σ_2 two more times. Panel (b) shows the intersection curves of R_4 (red) and R_7 (green) with Σ_2. Note that we again show the rescaled variable $\hat{c}$ on the horizontal axis to make the intersection curves distinguishable. The red intersection curve $R_4 \cap \Sigma_2$ is that from Fig. 8(b). The black dots correspond to the stable periodic orbit Γ. The closed green curve consists of the third and fourth intersections of R_7 with Σ_2, and it is extremely close to $R_4 \cap \Sigma_2$; panel (c) shows a schematic sketch of panel (b), illustrating that the green curve is actually closed and nested inside the closed red curve. Moreover, we found that the third and fourth returns of all ribbons R_1–R_7 are also extremely close to $R_4 \cap \Sigma_2$, as are the fifth to eighth returns of R_7. This is because trajectories of ribbons R_1–R_7 are

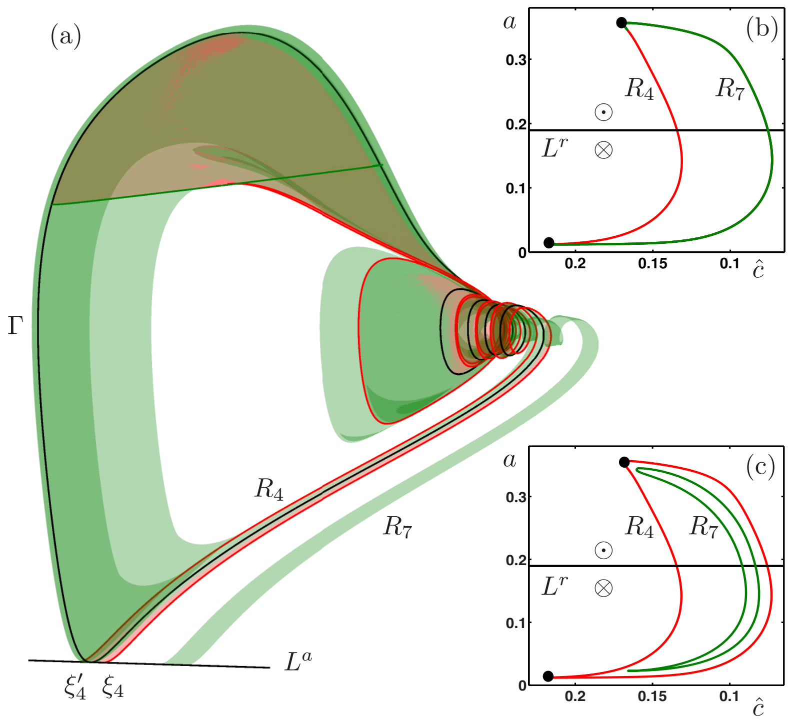

Figure 9: The extended ribbons R_7 and R_4. Panel (a) shows a part of R_7 (green) calculated up to its fourth return to Σ_2. The green curve corresponds to the third and fourth returns of the green surface to Σ_2. Also shown are R_4 (red) calculated up to its second return to Σ_2, the twin canards ξ_4 and ξ_4' (red curves), and the periodic orbit Γ (black). Panel (b) shows the computed intersection curves of R_4 and R_7 with Σ_2, where we used the rescaled variable $\hat{c}$; panel (c) is a sketch that shows the location of $R_7 \cap \Sigma_2$ relative to the computed intersection $R_4 \cap \Sigma_2$. The red curve segments above and below L^r correspond to the first and second returns of R_4 to Σ_2, respectively. The green curve segments above and below L^r correspond to the third and fourth returns of R_4 to Σ_2, respectively. The two black dots correspond to Γ.

converging to the attracting periodic orbit $\Gamma \subseteq R_4$.

3.2 Intermediate ribbons

Guckenheimer and Scheper [22] studied the return map of system Eq. (1) to a section $\Sigma_\mu := \left\{(a, b, c) \in \mathbb{R}^3_+ |\ b = 5\mu/(2-2\mu)\right\}$ that contains the equilibrium of system Eq. (1); they used this one-dimensional map extensively to study the transitions between different MMOs. They were successful in constructing approximate one-dimensional return and induced maps due to the strong contraction to the attracting slow manifold. In the same spirit, we construct a flow map $\Psi : c_0 \to a_1$, where c_0 denotes the c-coordinates of the initial points on L^a and a_1 denotes the a-coordinates of the end points on Σ_2. This flow map is computed by finding the actual orbit segments that satisfy the corresponding boundary conditions. Since one end point lies on L^a, such orbit segments lie on the extended attracting slow manifold. Therefore, we can use the map Ψ to understand the global structure of the ribbons on the extended attracting slow manifoldfs, each of which corresponds to a branch of Ψ. The flow map Ψ

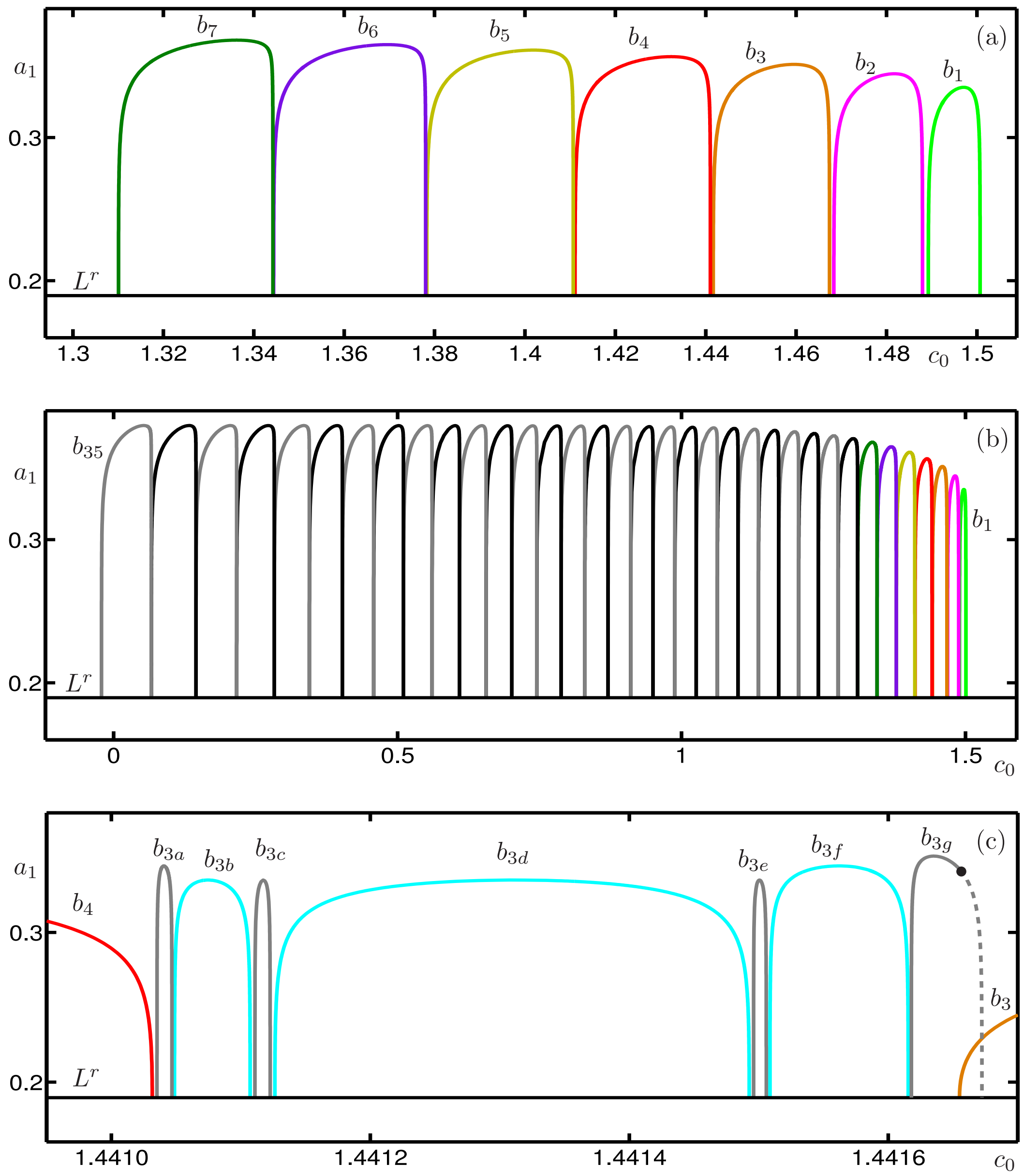

Figure 10: The graph of the flow map Ψ. Plotted are the first returns to Σ_2 versus the initial points on L^a. Panel (a) shows the branches b_1–b_7 corresponding to the ribbons R_1–R_7. The horizontal line L^r represents the a-value of the tangency locus of Σ_2. Panel (b) shows all main branches b_1–b_{35}. Panel (c) shows seven of the intermediate branches b_{3a}–b_{3g} that lie in between b_3 and b_4.

is also useful for understanding the mechanism of creating the LAOs. Figure 10(a) shows the graph of Ψ; that is, the a-values a_1 of first returns to Σ_2 are plotted versus the c-values c_0 of initial points on L^a. The black horizontal line L^r represents the locus of tangency of Σ_2, which lies at $a_1 = 0.191352$. Plotted are seven branches b_1–b_7 that correspond to ribbons R_1–R_7; compare with figures 6 and 7. The branches b_1–b_7 do not overlap and each branch is bounded by a corresponding pair of twin canard orbits which are the end points of these branches. Note that the branches b_1–b_7 have already been shown in Fig. 6(b) but in

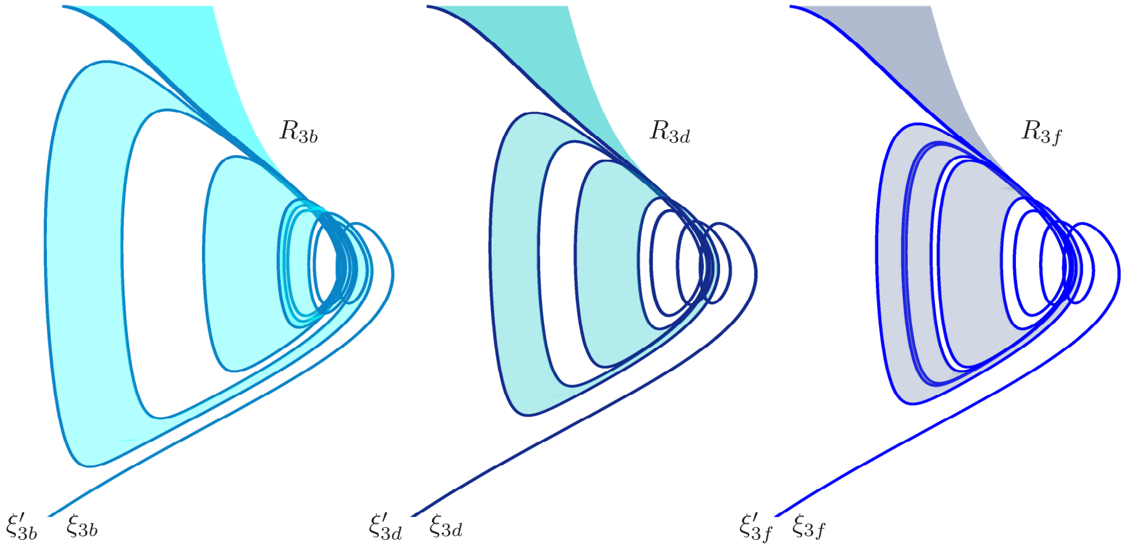

Figure 11: Three intermediate ribbons R_{3b}, R_{3d} and R_{3f} that lie in between R_3 and R_4 and correspond to the branches b_{3b}, b_{3d} and b_{3f} shown in Fig. 10(b), respectively. These ribbons are also bounded by twin canard orbits (thick curves).

a different way, namely, as intersection curves in Σ_2.

We find more than 35 ribbons, each bounded by a pair of twin canard orbits. Figure 10(b) shows 35 branches of Ψ that correspond to 35 main ribbons. The colored branches are those shown in panel (a), and branches b_8–b_{35} are alternately colored black and gray. Note that a part of b_{35} includes negative values of c_0, which violates the physical restriction $c > 0$. In between every two neighboring branches in Fig. 10(b), there is a gap. In each such gap, we find additional branches of Ψ, which we call intermediate branches. These branches do not correspond to any of the main ribbons shown in panel (b). Note that an intermediate branch has a relatively small domain, namely, one that is well smaller than that of b_1. Figure 10(c) shows seven of the intermediate branches b_{3a}–b_{3g} of Ψ, alternately colored cyan and gray, that lie in between b_3 and b_4. These intermediate branches were computed individually by starting from L^a between b_3 and b_4 and ending on Σ_2. Between every two intermediate branches, there also exist more branches. Each intermediate branch corresponds to a family of trajectories of S^a_ε that have a certain number of SAOs and form a ribbon that is bounded by a pair of twin canard orbits. Note that b_{3g} ends at the black dot, which has the same c_0-value as the end point of b_3 and represents its second return to Σ_2. In other words, when extending the canard orbit corresponding to the end point of b_3, it makes a global return to the attracting slow manifold and then makes three SAOs before intersecting Σ at the black dot. The dashed part of b_{3g} represents the third returns of b_3 to Σ_2 for some c_0-interval. For this interval, trajectories of the dashed branch actually make two SAOs followed by one LAO and then three SAOs before intersecting Σ_2.

Figure 11 illustrates the three intermediate ribbons R_{3b}, R_{3d} and R_{3f} in between R_3 and R_4 that correspond to the branches b_{3b}, b_{3d} and b_{3f} shown in Fig. 10(c). These ribbons have six, five and six SAOs, respectively, in the vicinity of the fold. Hence, the number of SAOs does not change monotonically when moving between different intermediate ribbons. Furthermore, an orbit with i SAOs does not necessarily belong to the main ribbon R_i. The

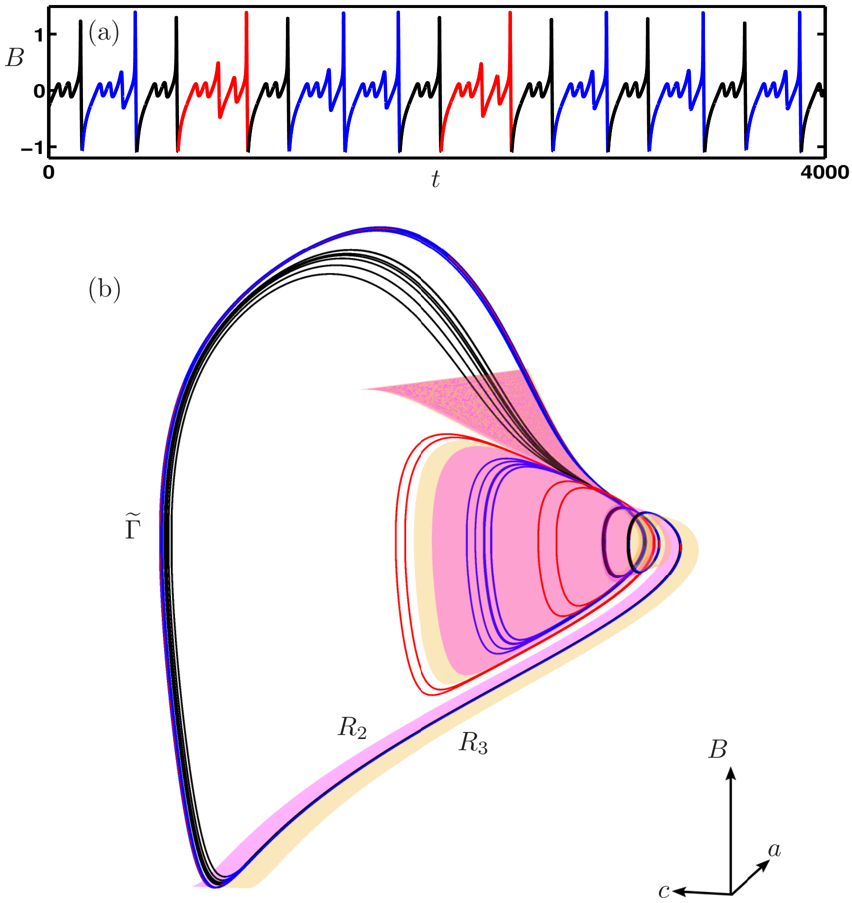

Figure 12: Illustration of a chaotic trajectory $\widetilde{\Gamma}$ for $\mu = 0.29628$, where black, blue and red correspond to segments with signatures 1^2, 1^3 and 1^4, respectively. Panel (a) is the time series and panel (b) shows $\widetilde{\Gamma}$ together with ribbons R_2 and R_3 in (a, c, B)-space.

twin canard orbits (thick curves) bounding these ribbons lie very close to each other along S^a_ε and S^r_ε but are well separated near F. The SAOs exhibited by the intermediate branches are relatively large. Nevertheless, we call them SAOs according to the following practical criterion. An oscillation with a maximum in B that is lower than Σ_2 is referred to as a SAO; otherwise we call it a LAO. Thus, trajectories of b_{3a}, b_{3c}, b_{3e} and b_{3f} have seven SAOs, trajectories of b_{3b} and b_{3g} have six SAOs and trajectories of b_{3d} have five SAOs.

The ribbons of the extended attracting slow manifold play a very important role in organizing the patterns of MMOs. Note from Fig. 2 that there are seven different coexisting unstable periodic orbits for $\mu = 0.295$. We found that these periodic orbits are guided by the ribbons of the extended attracting slow manifold. For example, a periodic orbit of type 1^i stays close to a ribbon R_i and makes i SAOs before making a large excursion and returning to the vicinity of R_i when closing. We also found that the ribbons of the extended attracting slow manifold persist for other values of μ and observed that they are associated with the corresponding signatures of MMOs. For instance, there exists a stable MMO with signature $1^1 1^2$ for $\mu = 0.2975$; see Fig. 1(b). This MMO stays close to R_1, makes one SAO, then a global return to R_2 exhibiting two SAOs, and finally a global return back to R_1 to close the orbit. Moreover, as we vary μ, we find that intermediate ribbons can be associated with chaotic behavior. Figure 12 shows a chaotic trajectory $\widetilde{\Gamma}$ for $\mu = 0.29628$ that alternates irregularly between signatures 1^2, 1^3 and 1^4. Panel (a) shows the time series of $\widetilde{\Gamma}$, which was produced after a long forward integration to allow transients to die down. The segments of the trajectory corresponding to signatures 1^2, 1^3 and 1^4 are colored black, blue and red, respectively. Panel (b) shows the same chaotic trajectory $\widetilde{\Gamma}$ in the three-dimensional (a, c, B)-space. Also shown are the ribbons R_2 and R_3 of the attracting slow manifold computed for $\mu = 0.29628$. We find that trajectory segments with signatures 1^2 and 1^3 indeed stay extremely close to R_2 and R_3, respectively. We also find that trajectory segments with signature 1^4 stay very close to the intermediate ribbons in between R_2 and R_3.

4 Termination/creation of twin canard orbits at fold bifurcations

We now investigate how twin canard orbits of system Eq. (7) depend on ε, and what the mechanism is for terminating/creating twin canard orbits. To this end, we continue each canard orbit with the same boundary value problem setup as in [12], that is, as an ε-dependent family of orbit segments that start on L^a and end on L^r; here L^a and L^r do not change with ε. Figure 13 shows the results of the continuation of canard orbits ξ_1–ξ_7 in ε, where we set $\mu = 0.295$ in system Eq. (7) as before. Panel (a) shows the continuation, in both directions, of the canard orbit ξ_4 only. The vertical axis is the L_2-norm of the orbit segment with respect to the coordinates a, B and c. We start from the green dot at $\varepsilon = 0.01$, which corresponds to ξ_4 shown in Fig. 7. In slight abuse of notation, we use ξ_4 and ξ_4' to denote the ε-dependent branches that correspond to the main twin canard orbits with four SAOs. The lower and upper red branches in panel (a) represent ξ_4 and ξ_4', respectively, for different ε-values. First, as ε is decreased, the lower branch ξ_4, converges to the strong singular canard near the singular limit and the amplitudes of the SAOs go to zero; as soon as ε is small enough, the folded node p, discussed in section 2, and its associated funnel region are responsible for the creation of ξ_4, as is expected from the theory [42, 44].

When continuing the red branch from the green dot for increasing ε, the branch ξ_4 encounters a fold and meets ξ_4' along the upper part of the red branch. Hence, the pair of twin canard orbits ξ_4 and ξ_4' merge at a fold bifurcation for $\varepsilon \approx 0.0107408$ and cease to exist for larger ε-values. The upper branch ξ_4' terminates at the black dot labeled (b2) in Fig. 13. To illustrate the termination of this branch, we select the canard orbits at the black dots labeled (b1), (b2) and (b3) and show each of them in the (c, B)-plane in the correspondingly labeled panels of Fig. 13. Panel (b1) shows the canard orbit ξ_4' for $\varepsilon = 8.6 \times 10^{-3}$. Note that the fourth SAO is already larger than the other three SAOs. Panel (b2) shows the canard orbit for $\varepsilon \approx 6.63471 \times 10^{-3}$, where the fourth SAO has increased so much in amplitude that it touches Σ_2. At this moment, we say that the fourth SAO has become a LAO, according to the criterion given in Section 3.2. Recall that L^r is the tangency locus in Σ_2. By our choice of L^r, the moment at which ξ_4' has a (local) B-maximum that is tangent to Σ_2, this maximum must lie on $L^r \subseteq \Sigma_2$. We no longer refer to the orbit shown in panel (b2) as the twin canard ξ_4'. Rather, this orbit is now a concatenation of a canard orbit with three SAOs, as ξ_3, and a canard orbit similar to ξ_0 with no SAOs. We refer to this type of orbit as a *composite canard*, defined as an orbit consisting of two canard segments that are connected

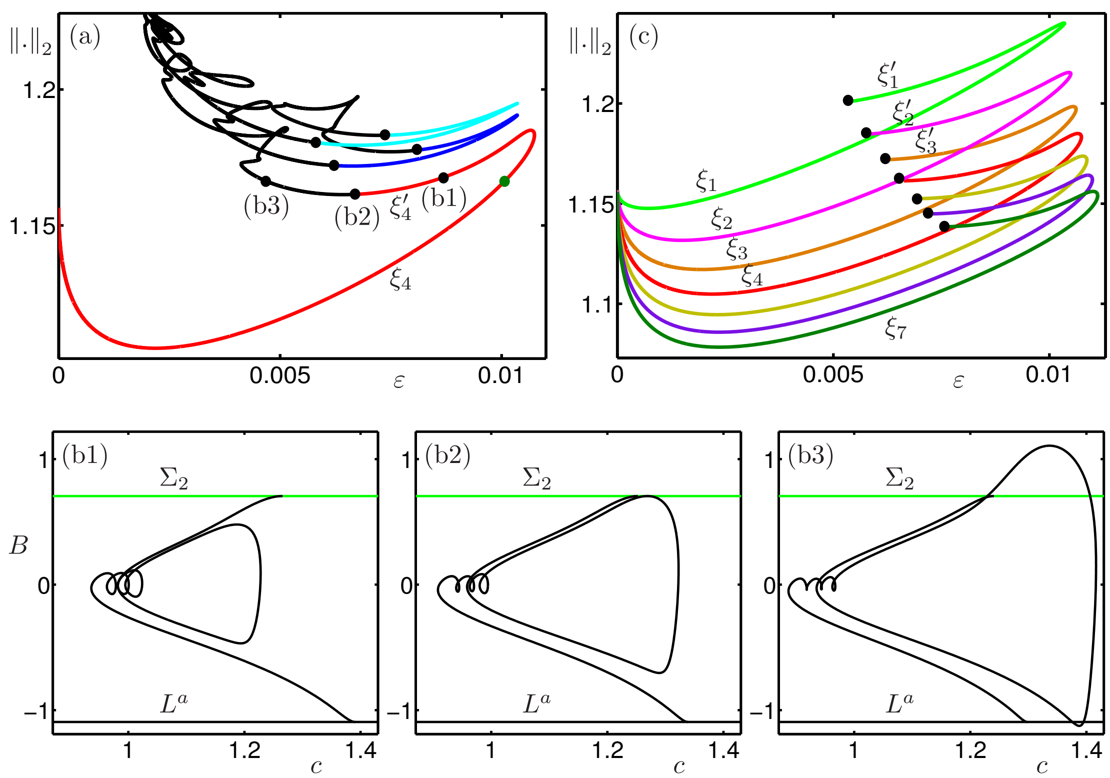

Figure 13: Continuation in ε of canard orbits ξ_1–ξ_7 with $\mu = 0.295$ in system Eq. (7). Panel (a) shows the continuation of ξ_4, where the L_2-norm is plotted versus ε. The red branch represents the main twin canard orbits ξ_4 and ξ_4'. The blue and cyan branches represent intermediate twin canards which also exhibit four SAOs. The black branch represents canard orbits with different numbers of small oscillations. The green dot corresponds to the canard orbit ξ_4 shown in Fig. 7. From left to right, panel (b) shows the canard orbit in the (c, B)-plane for $\varepsilon = 8.6 \times 10^{-3}$ before, $\varepsilon = 6.63471 \times 10^{-3}$ approximately at, and $\varepsilon = 4.6 \times 10^{-3}$ after the occurrence of the composite canard, where a SAO becomes a LAO. The green and black lines are the projection of Σ_2 and L^a, respectively. Panel (c) shows the continuation of ξ_1–ξ_7 up to their respective termination points, where the L_2-norm is plotted versus ε.

by a fast segment [12, 37]. In other words, at point (b2) in Fig. 13(a), the twin canard ξ_4' ceases to exist and the corresponding orbit segment becomes a composite canard that has a LAO. We refer to such a point as the termination point of the twin canard, in this case of ξ_4'.

Finally, Fig. 13(b3) shows the canard orbit for $\varepsilon = 4.6 \times 10^{-3}$, which clearly crosses Σ_2 makes a large excursion and a global return to the attracting slow manifold. As we decrease ε past (b3) in Fig. 13(a), the black branch encounters a number of termination points (not labeled). Hence, the oscillations of the continued canard orbit grow and shrink in size along the black branch, and have a mix of SAOs and LAOs. The precise sequence of transitions that occur along this branch is very complicated and are beyond the scope of this paper. However, there is a large diversity of coexisting canard orbits for $\varepsilon > 0.002$.

Note that there are two other branches of canard orbits, colored blue and cyan in Fig. 13(a1). Each of these branches corresponds to a pair of intermediate twin canard orbits that also have four SAOs. The intermediate twin canard orbits of the blue and cyan branches lie in between ribbons R_2 and R_3, and in between R_1 and R_2, respectively. Both branches exhibit a fold bifurcation for $\varepsilon = \mathcal{O}(10^{-2})$ and end at termination points (black dots) at which a SAO becomes tangent to $L^r \subseteq \Sigma_2$. More details on the continuation of intermediate canard orbits will be presented in Section 4.3.

Figure 13(c) shows the continuation of the seven canard orbits ξ_1–ξ_7, where we stopped each run at the respective termination point of the twin canard (black dots) where one of the SAOs becomes tangent to $L^r \subseteq \Sigma_2$. Note that the bifurcation structure is the same for all canard orbits shown. All branches can be continued to $\varepsilon = 0$ and the corresponding canard orbits all converge to the strong singular canard ξ_s as $\varepsilon \to 0$. Furthermore, all branches exhibit a fold bifurcation for $\varepsilon = \mathcal{O}(10^{-2})$ at which twin canard orbits are terminated/created. For each branch, twin canard orbits exist in the parameter interval between the fold and the respective termination point. Hence, the associated ribbons of the attracting slow manifold only exist in this parameter interval.

Continuation in ε of canard orbits have also been performed for the reduced Hodgkin-Huxley model and the self-coupled FitzHugh-Nagumo model [12, 20]. In both studies, it was found that, for decreasing ε, the canard orbits also converge to the strong singular canard as $\varepsilon \to 0$. Moreover, the canard orbits also exhibit fold bifurcations as ε is increased. In particular, sets of twin canard orbits have been reported in [20, Figure 3].

4.1 The mechanism for the tangency of slow manifolds

To gain a better understanding of the termination/creation of twin canard orbits, it is useful to study the local geometry of the attracting and repelling slow manifolds S^a_ε and S^a_ε, respectively, near the fold of canard orbits. To this end, we consider a different section transverse to L^r, namely, $\Sigma_3 := \left\{(a,b,c) \in \mathbb{R}^3_+ \mid c = 1.1\right\}$. Figure 14 illustrates the interaction of S^a_ε and S^r_ε with the section Σ_3, for $\varepsilon = 0.010724$ before, $\varepsilon \approx 0.0107408$ at, and $\varepsilon = 0.010756$ after the fold of canard orbits, in panels (a), (b) and (c), respectively. The top row shows local pieces of S^a_ε (red surface) and S^r_ε (blue surface) and the section Σ_3 (green). The bottom row shows the corresponding intersection curves $S^a_\varepsilon \cap \Sigma_3$ (red) and $S^r_\varepsilon \cap \Sigma_3$ (blue) in Σ_3. Panel (a) illustrates how S^a_ε and S^r_ε intersect transversely in two curves. These curves are the twin canard orbits ξ_4 (brown) and ξ'_4 (green), both of which have four SAOs. The canard orbit ξ_4 is taken from the data shown in Fig. 13(a), and it was also used as an initial orbit for the computed orbits of both S^a_ε and S^r_ε. Panel (b) displays the local interaction between S^a_ε and S^r_ε at the fold of canard orbits, where these manifolds are tangent to each other along the canard orbit ξ^*_4 (black orbit) with four SAOs. In panel (c), the surfaces S^a_ε and S^r_ε scroll around each other without intersecting.

The evolution of the curves $S^a_\varepsilon \cap \Sigma_3$ and $S^a_\varepsilon \cap \Sigma_3$ can be visualized in (ε, a, B)-space as an interaction between two-dimensional surfaces $(S^a_\varepsilon \cap \Sigma_3)(\varepsilon)$ and $(S^r_\varepsilon \cap \Sigma_3)(\varepsilon)$. This different view of the tangency of slow manifolds is provided in Fig. 15 by showing the surfaces $(S^a_\varepsilon \cap \Sigma_3)(\varepsilon)$ (red) and $(S^r_\varepsilon \cap \Sigma_3)(\varepsilon)$ (blue) for the interval $\varepsilon \in [0.01065, 0.01075]$. Note that the two surfaces intersect transversally in a nice parabolic curve (black). This parabolic nature of the curve corresponds to the intersection points of the twin canard orbits ξ_4 and ξ'_4 with Σ_2. The parabolic nature of the curve indicates that the fold bifurcation corresponds to a generic quadratic tangency of the two slow manifolds, as expected. Figure 15 also shows representative curves of $(S^a_\varepsilon \cap \Sigma_3)(\varepsilon)$ (magenta) and $(S^r_\varepsilon \cap \Sigma_3)(\varepsilon)$ (cyan) for constant ε before, at, and after the fold bifurcation of canard orbits.

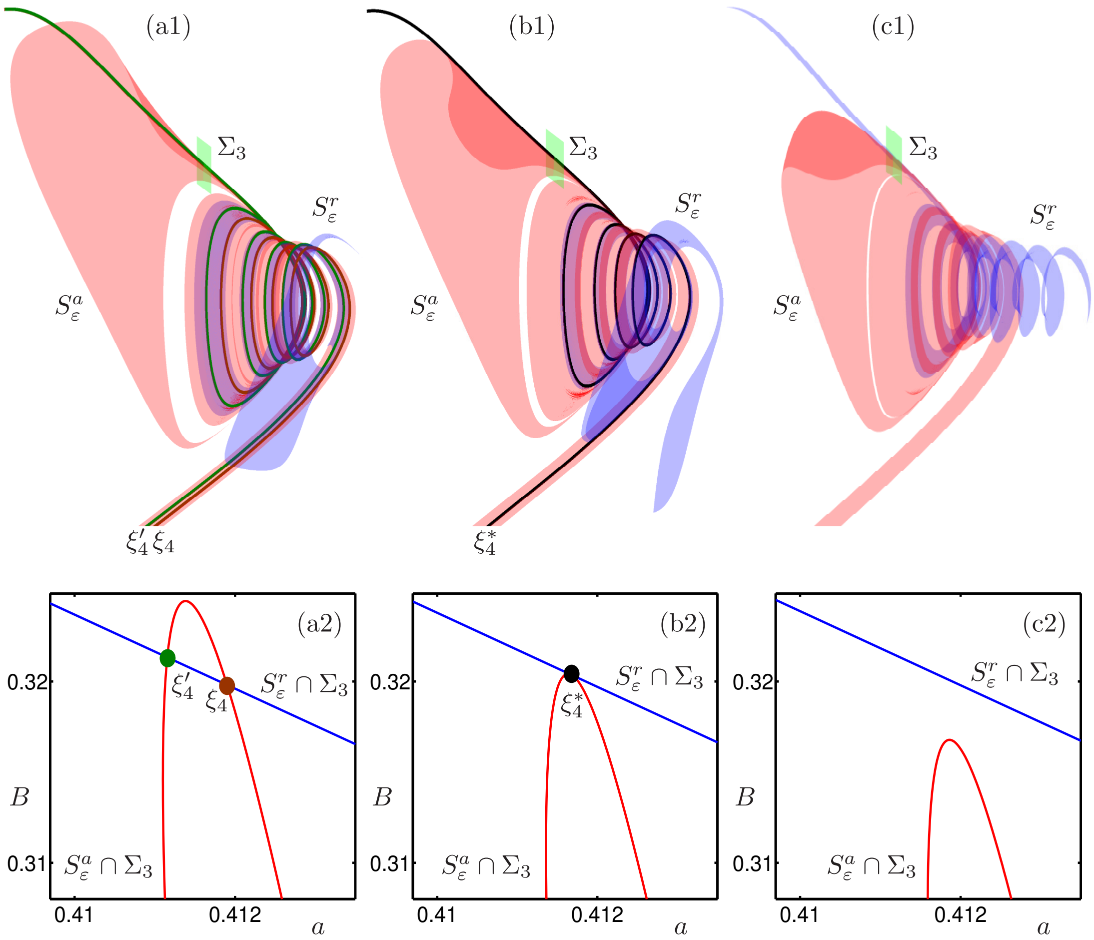

Figure 14: Illustration of the fold bifurcation of ξ_4 and ξ_4', and S^a_ε and S^r_ε. Shown are local interactions between S^a_ε and S^r_ε for $\varepsilon = 0.010724$ before (a), $\varepsilon \approx 0.0107408$ at (b), and $\varepsilon = 0.010756$ after (c) the fold. The top row shows the interactions between S^a_ε (red surface) and S^r_ε (blue surface). The green plane is the section Σ_3. Green, brown and black curves are intersections of $S^a_\varepsilon$and S^r_ε (canard orbits). The bottom row shows the corresponding intersection curves S^a_ε (red) and S^r_ε (blue) with Σ_3. Red and blue curves represent $S^a_\varepsilon \cap \Sigma_3$ and $S^r_\varepsilon \cap \Sigma_3$, respectively. Here, we fix $\mu = 0.295$.

4.2 Continuation of all main canard orbits

For $\varepsilon = 0.01$, we found 35 main ribbons that are bounded by twin canard orbits; see Fig. 10(b). We continued all of these canard orbits in ε. As before, the continuation was done in both directions and the computation was stopped at the respective termination points. Figure 16 shows the branches of canard orbits ξ_0–ξ_{28}. The colored branches ξ_1–ξ_7 are those shown in Fig. 13(c), and branches ξ_8–ξ_{28} are alternately colored black and gray; the termination points are marked by black dots. We find that the branches of canard orbits ξ_1–ξ_{20} can all be continued to $\varepsilon = 0$, and the respective canard orbits all converge to the strong singular canard orbit ξ_s in the limit as $\varepsilon \to 0$. Computationally, the branches ξ_{21}–ξ_{28} do not reach the singular limit. However, theoretically, we expect all of these branches to end at $\varepsilon = 0$ and their corresponding canard orbits also converge to ξ_s. Figure 16 also shows a the branch associated with the primary strong canard ξ_0 from Fig. 5 that has no SAOs.

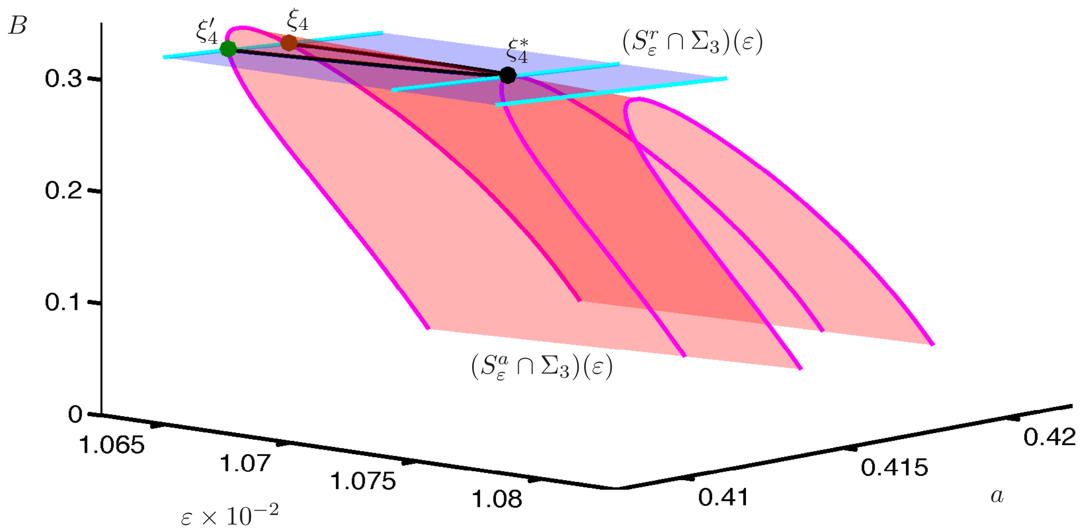

Figure 15: Continuation of local intersection curves of the attracting S^a_ε (red) and repelling S^r_ε (blue) slow manifolds with Σ_3 for different values of ε. The black curve is the ε-dependent intersection curve between $S^a_\varepsilon \cap \Sigma_3(\varepsilon)$ and $S^r_\varepsilon \cap \Sigma_3(\varepsilon)$. The magemta and cyan curves are representative intersection curves $S^a_\varepsilon \cap \Sigma_3$ and $S^r_\varepsilon \cap \Sigma_3$, respectively, for $\varepsilon = 0.01075$ before, $\varepsilon \approx 0.0107408$ at, and $\varepsilon = 0.01065$ after the fold bifurcation of canard orbits; compare with Fig. 14. Here, we fix $\mu = 0.295$.

This branch extends all the way to large values of ε without going through any folds. We remark that, for sufficiently large ε, the orbit segment corresponding to this branch loses its slow-fast nature and no longer stays close to the critical manifold.

Figure 17(a) shows the continuation of ξ_{29}–ξ_{35}. As ε is increased, all branches exhibit fold bifurcations and then termination points where the continuation is stopped. For decreasing ε, branches ξ_{29}–ξ_{35} again exhibit fold bifurcations before diverging in norm. Recall that canard theory [42, 44] predicts the existence of 29 secondary canard orbits for $\mu = 0.295$ near the singular limit of ε. We indeed find that ξ_{30}–ξ_{35} do not exist near the singular limit for this value of μ. Our numerical results suggest that when continuing the branch of ξ_{29} for decreasing ε, this branch also goes through a fold bifurcation without converging to the singular limit. To investigate the mechanism for this fold bifurcation, panels (b)–(d) of Fig. 17 show the canard orbits that correspond to the three labeled points on the branch ξ_{29} for $\varepsilon = 0.005411$ before, $\varepsilon = 0.00470645$ at, and $\varepsilon = 0.00476068$ after the left fold bifurcation. The first and second rows of panels (b)–(d) show the transformed canard orbit on the (c, B)-plane and on the (a, B)-plane, respectively. In order to understand the transformation of the canard orbit, we do not enforce the restriction $c > 0$. Panel (b) shows the canard orbit ξ_{29} before the fold bifurcation. The orbit follows the attracting slow manifold and then makes 29 SAOs before reaching L^r. Here, at the starting point of ξ_{29}, the sign of $\dot{a}$ is positive. Hence, the canard orbit is initially increasing in B and then follows the attracting slow manifold. Panel (c) shows the canard orbit ξ_{29} at the fold bifurcation. Here, the canard orbit starts at the intersection point of L^a with the a-nullcline ($\dot{a} = 0$), namely, at $(a, B, c) \approx (0.0799375, -1.094447, -2.22727)$. Therefore, this fold bifurcation is

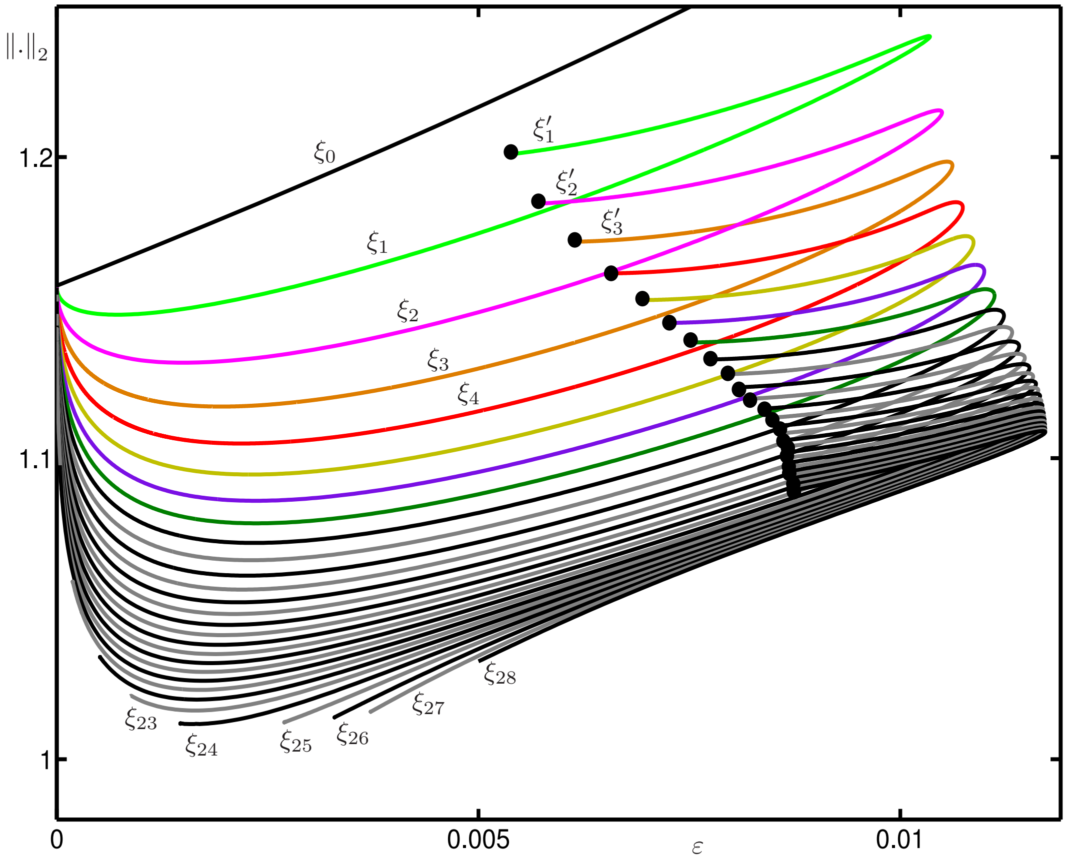

Figure 16: Continuation in ε of canard orbits ξ_0–ξ_{28}, with $\mu = 0.295$ in system Eq. (7). Continuation branches of ξ_1–ξ_7 are shown in different colors as in Fig. 13(c). Branches of ξ_8–ξ_{28} are alternately colored black and gray.

due to a tangency between the canard orbit and the a-nullcline at the starting point of the canard orbit. The orbit in panel (c) initially appears to be flat in both B- and a-directions (tangent to L^a), but eventually increases in B and follows the attracting slow manifold. Panel (d) shows the transformed canard orbit after the fold bifurcation. The canard orbit starts at a point with $\dot{a} < 0$. Hence, the canard orbit initially moves to the other side of the critical manifold and decreases in B along the slow flow. It then crosses the critical manifold at $B \approx -1.450973$ and increases in B following the attracting slow manifold. As we follow the branch ξ_{29} past the point labeled (c) in Fig. 17(a), the corresponding orbits initially decrease in B before crossing the critical manifold and forming canard orbits with 29 SAOs; see Fig. 17(d). This transition through a fold bifurcation is representative of the other branches ξ_{30}–ξ_{35} of panel (a).

4.3 Continuation of the intermediate canard orbits

We now discuss the continuation of intermediate canard orbits which bound intermediate ribbons in Fig. 11. Figure 18 shows the continuation of two branches of intermediate canard orbits. The black dots correspond to termination points. At these dots, one of the SAOs of the canard orbits become large and the canard orbit deforms into a composite canard

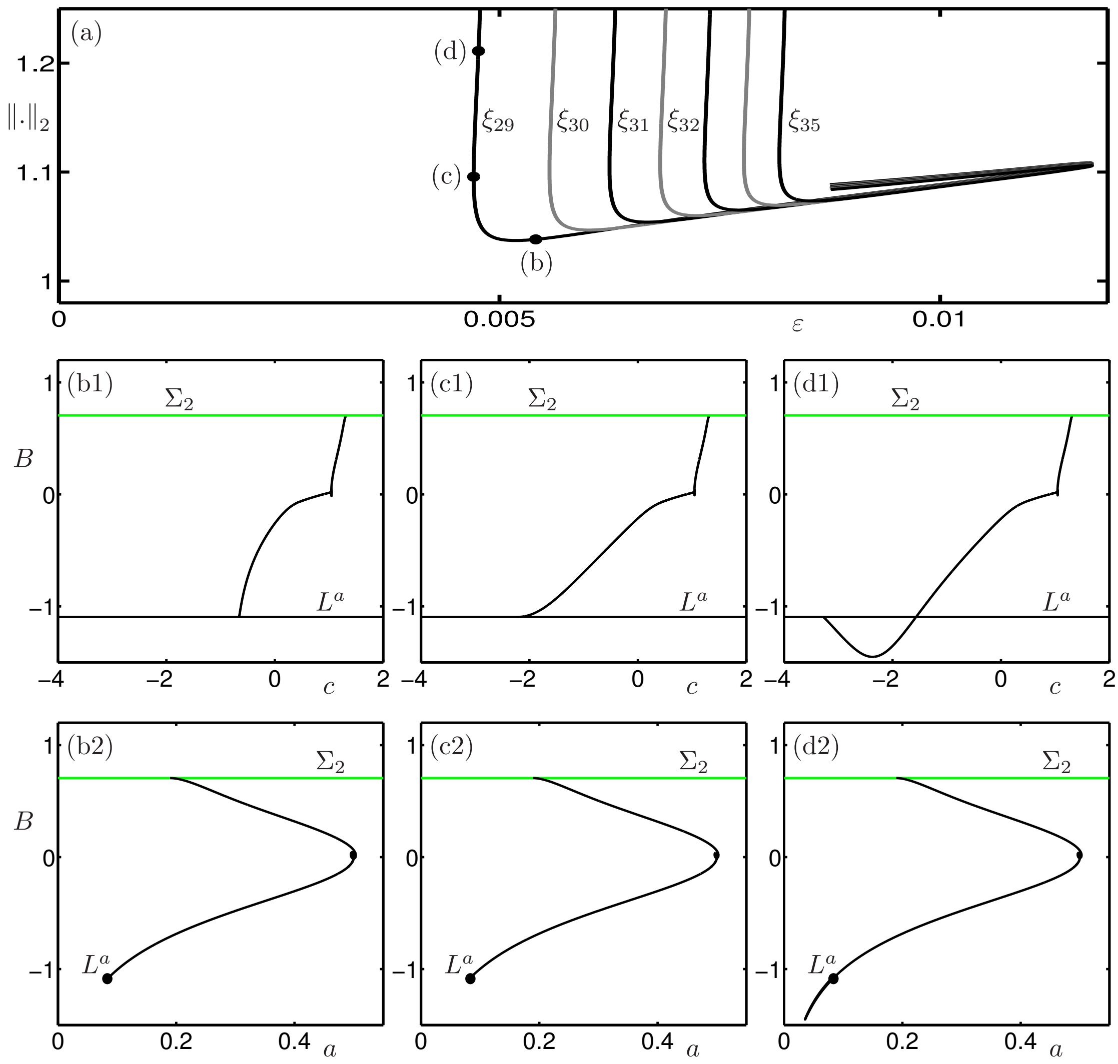

Figure 17: Continuation in ε of canard orbits ξ_{29}–ξ_{35}, with $\mu = 0.295$ in system Eq. (7). Panel (a) shows the continuation branches of ξ_{29}–ξ_{35}, alternately colored black and gray. Panels (b)–(d) show the transformed canard orbits ξ_{29} for $\varepsilon = 0.005411$ before, $\varepsilon = 0.00470645$ at and $\varepsilon = 0.00476068$ after the left fold bifurcation, as labeled in panel (a). The first and second rows of panels (b)–(d) show the transformed orbits in the (c, B)- and (a, B)-planes, respectively.

orbit; see, for example, Fig. 13(b2). Panel (a) shows the continuation of the intermediate canard orbits ξ_{3f} and ξ'_{3f}, which have six SAOs and bound the ribbon R_{3f} in Fig. 11 that lies in between ribbons R_3 and R_4. Here, we started the continuation from ξ_{3f} of Fig. 11 which is represented by the green dot in Fig. 18. We find that the continuation branch goes through a number of fold bifurcations before coming back to the starting point to form an isolated branch (isola). The upper and lower parts of the blue branch correspond to the intermediate twin canards ξ'_{3f} and ξ_{3f}, respectively. The cyan curve represents another pair of intermediate twin canards that also have six SAOs. We find that these twin canard orbits bound an intermediate ribbon that lies in between ribbons R_2 and R_3.

Figure 18(b) shows the continuation of intermediate canard orbits ξ_{3d} and ξ'_{3d} that have

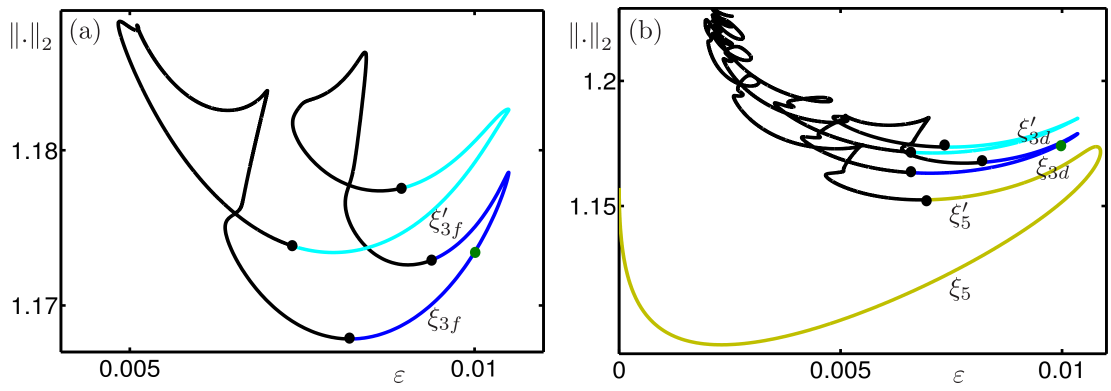

Figure 18: Continuation in ε of intermediate canard orbits ξ_{3f} and ξ_{3d} from Fig. 11, with $\mu = 0.295$; the L_2-norm is plotted versus ε. The black dots correspond to termination points. The blue branches correspond to the intermediate canard orbits ξ_{3f} in panel (a) and ξ_{3d} in panel (b). The cyan branches correspond to other intermediate canard orbits. The yellow branch corresponds to the main twin canard orbits ξ_5 and ξ'_5.

five SAOs and bound the ribbon R_{3d} in Fig. 11, which also lies in between ribbons R_3 and R_4. Note that the bifurcation diagram has the same qualitative structure as that for ξ_4 in Fig. 13(a), but here, the computation corresponds to the continuation of branch ξ_5, which was started from the intermediate canard orbit (green dot). The upper and lower parts of the blue curve correspond to the intermediate twin canards ξ'_{3d} and ξ_{3d}. The cyan curve corresponds to another pair of intermediate twin canards which also have five SAOs. These twin canard orbits bound an intermediate ribbon that lies in between ribbons R_2 and R_3. The yellow curve is the same branch of the twin canards ξ_5 and ξ'_5 shown in Fig. 13 and Fig. 16. For the blue and cyan branches, the respective intermediate canard orbits merge at fold bifurcations and cease to exist at termination points where a SAO becomes tangent to Σ_2. In both cases, we find that the branches of intermediate twin canards connect with branches of other twin canards with the same number of SAOs.

5 Conclusions and Discussion

We studied an autocatalytic chemical reaction model [22, 33, 36], which takes the form of a dynamical system with an explicit parameter ε that describes the time-scale ratio between one fast and two slow variables. Our goal was to investigate the mechanisms that underlie mixed-mode oscillations in a parameter regime where ε is too large to the immediate application of established results from the theory of slow-fast systems [7, 15, 25, 42, 44]. By computing slow manifolds and the associated canard orbits, we found that the system features twin canard orbits, which are co-existing canard orbits that exhibit the same number of small-amplitude oscillations. Twin canard orbits arise due to tangencies of attracting and repelling slow manifolds and do not exist near the singular limit ($\varepsilon = 0$). Twin canard orbits divide the (extended) attracting slow manifold into ribbons. These ribbons and their associated bounding twin canard orbits are characterized by their given number of SAOs. We distinguish between the main ribbons that have relatively large domains and intermediate ribbons that exist in the small gaps between neighboring main ribbons. The complicated structure of the ribbons and the associated canard orbits organizes the underlying patterns of MMOs.

Overall, we obtained a comprehensive picture of the geometry of MMOs for larger values of ε. Specifically, we found a total of 70 (main) canard orbits bounding main ribbons as well as further canard orbits bounding intermediate ribbons. Continuations of these canard orbits for decreasing ε revealed that 29 of them converge to the strong singular canard in the limit as $\varepsilon \to 0$, while the other canard orbits cannot be continued to the singular limit. When continuing them in the other direction, we found that the canard orbits exhibit fold bifurcations. These folds correspond to quadratic tangencies between the attracting and repelling slow manifolds, which is the mechanism that gives rise to a pair of canard orbits. Such fold bifurcations are a generic feature. They have been reported before in the self-coupled FitzHugh-Nagumo model [12, 20] and the reduced Hodgkin-Huxley model [12], but their significance in generating twin canard orbits was not recognized. For the self-coupled FitzHugh-Nagumo model [12, 20], these twin canard orbits only exist in the region of phase space where the model is not valid. For the reduced Hodgkin-Huxley model [12] it seems that all twin canard orbits can be continued back to the singular limit $\varepsilon = 0$, during which they transform into composite canards, where one SAO has become a LAO. For the autocatalator model Eq. (1), we similarly find that the twin canard orbits transform into composite canards, but the branch does not return to the singular limit $\varepsilon = 0$. Rather, there are additional folds that 'undo' this transition so that there are co-existing segments on the continuation branch where the (twin) canard orbits have the same signatures.

In the context of MMOs, it is a general challenge to provide an appropriate definition for when an oscillation has a small or large amplitude, respectively. We proposed a practical criterion for distinguishing between SAOs and LAOs in systems with one fast and two slow variables. We considered a fixed section transverse to the critical manifold sufficiently far away from the fold curve that separates the attracting and repelling sheets. Throughout the paper, oscillations that are below and above this threshold section were referred to as SAOs and LAOs, respectively. A transition between SAOs and LAOs occurs when an oscillation becomes tangent to the considered threshold section, which also determines the termination points of twin canard orbits. Although the choice of its position is not unique, moving the threshold section slightly will affect the results only quantitatively but not qualitatively. In particular, folds and termination points of twin canard orbits will persist. The section was chosen to contain the line used in the computation of the repelling slow manifold, which was in turn chosen so that the orbit segments stay close to the critical manifold the longest before reaching the fold curve. It turned out that this is a good choice for distinguishing between SAOs and LAOs.

The numerical techniques used in this paper are based on the definition of suitable two-point boundary value problems [26], which are then solved by the collocation method implemented in the continuation software package AUTO [13]. More specifically, we use this setup to compute suitable families of orbit segments. Our calculations have the advantage of giving robust results despite the sensitivity and stiffness due to the difference in time scales. We represented slow manifolds by families of orbit segments that start on the critical manifold sufficiently far away from the fold. Detecting canard orbits was challenging because there are multiple transversal intersections of slow manifolds with any section transverse to the fold curve. To overcome this challenge, we extended the attracting slow manifold up to a fixed section transverse to the critical manifold sufficiently far away from the fold curve. In this way, we successfully detected all canard orbits and associated ribbons in a systematic way.

It would be an obvious next step to revisit the continuations of canard orbits for the self-coupled FitzHugh-Nagumo model [12, 20] and the reduced Hodgkin-Huxley model [12]. Many realistic models of slow-fast systems feature more than three variables [1, 3, 8, 14, 24, 35, 39, 41, 45] and/or a different splitting of time scales. Therefore, an interesting direction for future work is to investigate such systems with different combinations of fast and slow variables; for example, systems with two fast and one slow, two fast and two slow or with a combination of fast, intermediate and slow variables. In particular, we believe that the idea of representing slow and invariant manifolds by families of orbit segments can also be applied in higher-dimensional slow-fast systems. While computing attracting and repelling slow manifolds in these situations is already quite a challenging task, such systems may also feature slow manifolds of saddle type with stable and unstable manifolds. Guckenheimer and Kuehn [21] presented an algorithm for computing one-dimensional slow manifolds of saddle type. In ongoing research, we are developing methods for computing one- and two-dimensional saddle slow manifolds, and their stable and unstable manifolds. Finally, many slow-fast systems have no explicit time-scale separation and may contain various regions with different splittings of time scales. The approach presented in this paper may also be helpful for the investigation of such more general systems.

Acknowledgments

We would like to thank John Guckenheimer for helpful discussions.

References

[1] C. D. Acker, N. Kopell, and J. A. White, *Synchronization of strongly coupled excitatory neurons: Relating network behaviour to biophysics*, J. Comput. Neurosci., 15 (2003), pp. 71–90.

[2] K. Al-Naimee, F. Marino, M. Ciszak, R. Meucci, and F. T. Arecchi, *Chaotic spiking and incomplete homoclinic scenarios in semiconductor lasers with optoelectric feedback*, New J. Phys., 11 (2009), 073022.

[3] D. Barkley, *Slow manifolds and mixed-mode oscillations in the Belousov-Zhabotinskii reaction*, J. Chem. Phys., 89 (1988), pp. 5547–5559.

[4] É. Benoît, *Systèmes lents-rapides dans* $\mathbb{R}^3$ *et leurs canards*, Astérisque, 109110 (1983), pp. 159–191.

[5] É. Benoît, *Canards et enlacements*, Inst. Hautes Études Sci. Publ. Math., 72 (1990), pp. 63–91.

[6] B. Braaksma, *Singular Hopf bifurcation in systems with fast and slow variables*, J. Nonlinear Sci., 8 (1998), pp. 457–490.

[7] M. Brøns, M. Krupa, and M. Wechselberger, *Mixed-mode oscillations due to the generalized canard phenomenon*, Fields Institute Communications., 49 (2006), pp. 39–63.

[8] T. R. Chay and J. Keizer, *Minimal model for membrane oscillations in the pancreatic β-cell*, Biophys. J., 42 (1983), pp. 181–190.

[9] M. Desroches, J. Guckenheimer, B. Krauskopf, C. Kuehn, H. M. Osinga, and M. Wechselberger, *Mixed-mode oscillations with multiple time scales*, SIAM Review 54:2, (2012), pp. 211–288.

[10] M. Desroches, B. Krauskopf, and H. M. Osinga, *The geometry of slow manifolds near a folded node*, SIAM J. Appl. Dyn. Syst., 7 (2008), pp. 1131–1162.

[11] M. Desroches, B. Krauskopf, and H. M. Osinga, *Mixed-mode oscillations and slow manifolds in the self-coupled FitzHugh-Nagumo system*, Chaos, 18 (2008), 015107.

[12] M. Desroches, B. Krauskopf, and H. M. Osinga, *Numerical continuation of canard orbits in slow-fast dynamical systems*, Nonlinearity, 23 (2010), pp. 739–765.

[13] E. J. Doedel, *Auto-07P: Continuation and bifurcation software for ordinary differential equations*, with major contributions from A. C. Champneys, T. F. Fairgrieve, Yu. A. Kuznetsov, B. E. Oldeman, R. C. Paffenroth, B. Sandstede, X. J. Wang, and Zhang C; available at http://cmvl.cs.concordia.ca/auto/.

[14] S. Doi, J. Inoue, and S. Kumagai, *Chaotic spiking in the Hodgkin-Huxley nerve model with slow inactivation in the sodium current*, J. Integr. Neurosci., 3 (2004), pp. 20–225.

[15] N. Fenichel, *Geometric singular perturbation theory for ordinary differential equations*, J. Differential Equations, 31 (1979), pp. 53–98.

[16] P. Gray, and S. K. Scott, *A new model for oscillatory behaviour in closed systems: The autocatalator*, Phys.Chem., 90 (1986), pp. 985–996.

[17] J. Guckenheimer, *Singular Hopf bifurcation in systems with two slow variables*, SIAM J. Appl. Dyn. Syst., 7 (2008), pp. 1355–1377.

[18] J. Guckenheimer and R. Haiduc, *Canards at folded nodes*, Mosc. Math. J., 5 (2005), pp. 91–103.

[19] J. Guckenheimer, R. Harris-Warrick, J. Peck, and A. R. Willms, *Bifurcation, bursting, and spike frequency adaptation*, J. Comput. Neurosci., 4 (1997), pp. 257–277.

[20] J. Guckenheimer, B. Krauskopf, H. M. Osinga and B. Sandstede, *Invariant manifolds and global bifurcations*, Chaos, 25 (2015), 097604.

[21] J. Guckenheimer and C. Kuehn, *Computing slow manifolds of saddle type*, SIAM J. Appl. Dyn. Syst., 8 (2009), pp. 854–879.

[22] J. Guckenheimer and C. Scheper, *A geometric model for mixed-mode oscillations in a chemical system*, SIAM J. Appl. Dyn. Syst., 10 (2011), pp. 92–128.

[23] I. Gucwa and P. Szmolyan, *Geometric singular perturbation analysis of an autocatalator model*, Discrete Contin. Dyn. Syst. — Ser. S, 2 (2009), pp. 783–806.

[24] L. Györgyi , R. J. Field, *Simple models of deterministic chaos in the Belousov-Zhabotinskii reaction*, J. Phys. Chem., 95, (1991), pp. 6594–6602.

[25] C.K.R.T. Jones, *Geometric singular perturbation theory*, in Dynamical Systems (Montecatini Terme, 1994), Springer-Verlag, New York, (1995), pp. 44–120.

[26] B. Krauskopf and H. M. Osinga, *Computing invariant manifolds via the continuation of orbit segments*, in Numerical Continuation Methods for Dynamical Systems: Path Following and Boundary Value Problems, B. Krauskopf, H. M. Osinga, and J. Galán-Vioque, eds., Springer-Verlag, Berlin, New York, 2007, pp. 117–154.

[27] B. Krauskopf, K. R. Schneider, J. Sieber, S. M. Wieczorek, and M. Wolfrum, *Excitability and self-pulsations near homoclinic bifurcations in semiconductor laser systems*, Optics Communications, 215 (2003), pp. 367–379.

[28] M. Krupa, N. Popović, N. Kopell, and H. G. Rotstein, *Mixed-mode oscillations in a three time-scale model for the dopaminergic neuron*, Chaos, 18 (2008), 015106.

[29] C. Kuehn, *Normal hyperbolicity and unbounded critical manifolds*, Nonlinearity, 27 (2014), pp. 1351–1366.

[30] C. M. Lee, P. J. Collins, B. Krauskopf and H. M. Osinga, *Tangency bifurcations of global Poincaré maps*, SIAM J. Appl. Dyn. Syst., 7 (2008), pp. 712–754.

[31] J. Maselko, and H. L. Swinney, *A Complex Transition Sequence in Belousov-Zhabotinskii Reaction*, Phys. Scripta, T9 (1985), pp. 35–39.

[32] J. H. Merkin, D. J. Needham, and S. K. Scott, *On the structural stability of a simple pooled chemical system*, J. Engng. Maths., 21 (1987), pp. 115–127.

[33] A. Milik, and P. Szmolyan, *Multiple time scales and canards in a chemical oscillator*, in Multiple-Time-Scale Dynamical Systems, C. Jones and A. Khibnik, eds., Springer-Verlag, New York, 2001, pp. 117–140.

[34] A. Milik, P. Szmolyan, H. Loeffelmann, and E. Groeller, *Geometry of mixed-mode oscillations in the 3-D autocatalator*, Internat. J. Bifur. Chaos Appl. Sci. Engrg., 8 (1998), pp. 505–519.

[35] L. F. Olsen. *An enzyme reaction with a strange attractor.* Physics Letters A, 94 (1983), pp. 454–457.

[36] B. Peng, S. K. Scott, and K. Showalter, *Period doubling and chaos in a three-variable autocatalator*, J. Phys. Chem., 94 (1990), pp. 5243–5246.

[37] C. Perryman and S. Wieczorek, *Adapting to a changing environment: Non-obvious thresholds in multi-scale systems*, Proc. R. Soc. A, 470 (2014), 20140226.

[38] V. Petrov, S. Scott, and K. Showalter, *Mixed-mode oscillations in chemical systems*, J. Chem. Phys., 97 (1992), pp. 6191–6198.

[39] J. Rubin and M. Wechselberger, *Giant squid-hidden canard: The 3D geometry of the Hodgkin-Huxley model*, Biol. Cyb., 97 (2007), pp. 5–32.

[40] J. Rubin and M. Wechselberger, *The selection of mixed-mode oscillations in a Hodgkin-Huxley model with multiple timescales*, Chaos, 18 (2008), 015105.

[41] J. V. Stern, H. M. Osinga, A. LeBeau, and A. Sherman, *Resetting behavior in a model of bursting in secretory pituitary cells: Distinguishing plateaus from pseudo-plateaus*, Bull. Math. Biol., 70 (2008), pp. 68–88.

[42] P. Szmolyan and M. Wechselberger, *Canards in* $\mathbb{R}^3$, J. Differential Equations, 177 (2001), pp. 419–453.

[43] D. Terman *Chaotic spikes arising from a model of bursting in excitable membranes*, SIAM J. Appl. Math., 51 (1991), pp. 1418–1450.

[44] M. Wechselberger, *Existence and bifurcation of canards in* $\mathbb{R}^3$ *in the case of a folded node*, SIAM J. Appl. Dyn. Syst., 4 (2005), pp. 101–139.

[45] M. Wechselberger and W. Weckesser, *Bifurcations of mixed-mode oscillations in a stellate cell model*, Phys. D, 238 (2009), pp. 1598–1614.